Comparison of ultrasonic attenuation within two- and three-dimensional polycrystalline media

X. Bai, B. Tie, Jean-Hubert Schmitt, D. Aubry

Comparison of ultrasonic attenuation within two- and three-dimensional polycrystalline media

X. Bai[a,b], B. Tie[a,*], J.-H. Schmitt[a], D. Aubry[a]

[a] *MSSMat Laboratory, CentraleSupélec, CNRS UMR8579, Université Paris-Saclay, 3 Rue Joliot Curie, 91190 Gif-sur-Yvette, France*
[b] *Laser Institute, Qilu University of Technology (Shandong Academy of Sciences), 250103, Shandong, China.*

Abstract

An analytical approach to develop explicit formulas of attenuation coefficient in both 2D and 3D cases is proposed. It results in a better understanding of the grain scattering mechanisms within a polycrystalline material and the grain size effects on the attenuation of an ultrasonic wave. It is based on the Stanke and Kino's model and uses the Born approximation. An explicit formula is deduced for untextured polycrystals with equiaxed grains of cubic symmetry and allows a rigorous comparison of the attenuation coefficient between both 2D and 3D cases. It confirms that the attenuation in the Rayleigh region is higher in 2D simulation than in 3D one, while very similar coefficients are obtained in the stochastic region for both cases. The study of the explicit formula allows the decomposition of the attenuation coefficient into various scattering-induced components, which leads to a better understanding of different grain scattering mechanisms. The reflection/transmission at grain boundaries between wave modes of a same type mainly explains a same attenuation coefficient in the stochastic region for both 2D and 3D modelings. The conversion at grain boundaries between different types of wave modes provides some explanations for a higher attenuation value given by the 2D modeling in the Rayleigh region. The effect of the grain size on the attenuation coefficient is then predicted by the 2D analytical calculation and by the FE simulation. The analytical-numerical comparison validates the numerical calculations and the approach suggests a way of using the 2D FE calculations to predict the evolution of the attenuation coefficient with the wave frequency in 3D.

Keywords: Finite element modeling; Ultrasonic attenuation; Grain scattering; Grain size effect; 2D/3D analytical modeling; Polycrystalline material

*Corresponding author
Email address: bing.tie@centralesupelec.fr (B. Tie)

1. Introduction

For on-line quality control both in laboratory and in industry, the amplitude attenuation of ultrasonic waves provides continuous and non-destructive information on polycrystalline microstructure [1–3]. It mainly results from scattering by grain boundaries delineating domains with different elastic properties, which, in the case of a single-phase polycrystal, are linked to crystallographic orientation. Depending on the ratio of the wavelength λ to the mean grain size d, three regions are usually defined: (1) the *Rayleigh scattering region* for $\lambda >> d$; (2) the *stochastic scattering region* for $\lambda \approx d$; (3) the *diffusion scattering region* for $\lambda << d$. The limits between the three regions depend upon the material properties and generally cannot be strictly specified [4, 5].

Early models for the attenuation were limited to the single-scattering approximation, assuming that ultrasonic waves scatter at each grain boundary independently [6–8]. This assumption is only valid for weak scattering. It may break down for strong scattering materials or at relatively high frequencies. Stanke and Kino [4] proposed a unified theory valid in all frequency regions by using the second-order Keller approximation [9]. Their approach took some degree of multiple scattering into account by writing the scattered field as an averaged field which has been scattered at grain boundaries. The unified theory resulted in a highly non-linear equation in the 3D case (see Eq.(101) and Eq.(102) in [4]). Instead of the perturbation theory used by Stanke and Kino, Weaver relied on the Dyson's equation to account for multiple-scattering through the self-energy operator [10]. When Born approximation is used, both Weaver's and Stanke and Kino's models gave rise to the same solution for the attenuation coefficients [11]. Extension of these two seminal models to polycrystalline materials with crystallographically textures [12], elongated grains [13], or a distribution of grain sizes [14] was investigated in the 3D case using the Born approximation. Though these ideas can be easily extended to the 2D case, it appears, to our knowledge, that no explicit formulas of attenuation coefficient were developed for the 2D case.

Some works indicate that a 2D approach is not fully representative of 3D scattering, particularly in the Rayleigh region and for the transition between the different scattering regions [15, 16]. For example, a scattering strengthening is observed in the Rayleigh region for 2D simulations. Consequently, a 2D theoretical model would be imperative for a further understanding of the dimensional behavior of ultrasonic scattering-induced attenuation. On another level, the numerical modeling is necessary to complement the analytical one [15, 17–20], and 2D finit element (FE) simulations are advantageous in their relative simplicity and efficiency compared to 3D ones while retaining the key concepts. A 2D theoretical model is thus of great significance to bring a better understanding of the limits of 2D calculations and to develop more efficient 2D simulations that can be representative of 3D phenomena.

In the following, Section 2 starts from the Stanke and Kino's model to give an explicit solution to the eigenvalue problem of the acoustic tensor. The Born approximation makes possible to obtain an explicit formula for the ultrasonic attenuation coefficient expressed as a simple integral form of the dyadic Green's tensor and a spatial correlation function for both 2D and 3D cases. Section 3 presents a quantitative comparison of attenuation coefficients calculated in 2D and 3D cases for an untextured and single-phase polycrystal with equiaxed grains of cubic symmetry. The contribution of different scattering mechanisms to the attenuation is also discussed to provide a physical interpretation to differences observed between the 2D and 3D cases. Finally, in Section 4, an example is given by the analysis of the effect of the grain size on the attenuation in a β-titanium polycrystal. 2D analytical predictions are compared with numerical results obtained by FE simulations.

2. Explicit formula of attenuation in single-phase untextured polycrystals

Considering a polycrystalline heterogeneous domain $\Omega \subset \mathbb{R}^{dim}$ $(dim = 2, 3)$ with boundary $\partial\Omega$ and defined by a position-dependent elastic tensor $\boldsymbol{C}(\boldsymbol{x})$ and a uniform density ρ. Let us assume that there is no source term, the time harmonic elastic wave equation inside Ω reads as:

$$\boldsymbol{L}(\boldsymbol{u}(\boldsymbol{x},\omega)) \equiv \rho\omega^2\boldsymbol{u}(\boldsymbol{x},\omega) + \boldsymbol{\nabla}_{\boldsymbol{x}} \cdot (\boldsymbol{C}(\boldsymbol{x}) : \boldsymbol{\varepsilon}_{\boldsymbol{x}}(\boldsymbol{u}(\boldsymbol{x},\omega))) = \boldsymbol{0} \tag{1}$$

In (1), $\boldsymbol{u}(\boldsymbol{x},\omega)$ denotes the Fourier transform with respect to time of the displacement field $\boldsymbol{u}(\boldsymbol{x},t)$, $\boldsymbol{\nabla}_{\boldsymbol{x}}$ the usual space gradient operator and $\boldsymbol{\varepsilon}_{\boldsymbol{x}}(\boldsymbol{u}(\boldsymbol{x},\omega)) = \boldsymbol{\nabla}_{\boldsymbol{x}} \otimes_s \boldsymbol{u}(\boldsymbol{x},\omega)$ the infinitesimal strain tensor. Herein, tensors and vectors are denoted using bold letters. Otherwise, ω in $\boldsymbol{u}(\boldsymbol{x},\omega)$ will be omitted in the following for the sake of simplicity.

Herein, the theoretical study is developed within the framework of the unified theory proposed by Stanke and Kino [4] following a general formulation established by Karal and Keller [9]. The objective is to develop an explicit model of $\langle \boldsymbol{u}(\boldsymbol{x}) \rangle$ the expected wave of an ensemble of possible inhomogeneous media, with $\langle \cdot \rangle$ denoting an ensemble average. For a particular inhomogeneous medium of the ensemble, its inhomogeneity degree can be quantified by considering the deviation of $\boldsymbol{C}(\boldsymbol{x})$ its elastic tensor from $\boldsymbol{C}^0$ the one of an equivalent homogeneous medium: $\delta\boldsymbol{C}(\boldsymbol{x}) = \boldsymbol{C}(\boldsymbol{x}) - \boldsymbol{C}^0$. Former work proved the equivalent homogeneous medium was to be chosen as the Voigt-averaged material of the ensemble [4, 10]. In the following, both the subscript and the superscript "0" always indicate fields or variables related to the equivalent homogeneous medium.

Following procedure described in [4, 9, 21], single-phase, untextured and weakly scattering polycrystals are considered. The untextured assumption leads

to $\langle \delta \boldsymbol{C}(\boldsymbol{x}) \rangle = \boldsymbol{0}$ and that of weak scattering means that the relative inhomogeneity degree ϵ is much less than 1. ϵ is defined by $\epsilon^2 = \langle (k(\boldsymbol{x}) - k_0)^2 \rangle / k_0^2$ with $\boldsymbol{k}$ the wave vector and $k = |\boldsymbol{k}|$ the propagation constant. Using the second-order Keller approximation, the following explicit equation for $\langle \boldsymbol{u}(\boldsymbol{x}) \rangle$ accurate to order of ϵ^2 can be obtained:

$$\boldsymbol{L}^0(\langle \boldsymbol{u}(\boldsymbol{x}) \rangle) - \langle \boldsymbol{L}^1(\int_\Omega \boldsymbol{G}^T(\boldsymbol{x}'; \boldsymbol{x}) \cdot \boldsymbol{L}^1(\langle \boldsymbol{u}(\boldsymbol{x}') \rangle) \, \mathrm{d}\boldsymbol{x}') \rangle = 0 \tag{2}$$

where $\boldsymbol{L}^0$ and $\boldsymbol{L}^1$ are respectively the homogeneous and perturbation operators defined by:

$$\boldsymbol{L}^0(\boldsymbol{u}(\boldsymbol{x})) = \rho \omega^2 \boldsymbol{u}(\boldsymbol{x}) + \boldsymbol{\nabla}_{\boldsymbol{x}} \cdot (\boldsymbol{C}^0 : \boldsymbol{\varepsilon}(\boldsymbol{u}(\boldsymbol{x}))) \tag{3a}$$

$$\boldsymbol{L}^1(\boldsymbol{u}(\boldsymbol{x})) = \boldsymbol{\nabla}_{\boldsymbol{x}} \cdot (\delta \boldsymbol{C}(\boldsymbol{x}) : \boldsymbol{\varepsilon}_{\boldsymbol{x}}(\boldsymbol{u}(\boldsymbol{x}))) \tag{3b}$$

In (2), $\boldsymbol{G}(\boldsymbol{x}'; \boldsymbol{x})$ is the dyadic Green function tensor defined by $\boldsymbol{G}(\boldsymbol{x}'; \boldsymbol{x}) = \boldsymbol{e}_m \otimes \boldsymbol{g}_m(\boldsymbol{x}'; \boldsymbol{x})$, $\boldsymbol{e}_m$ is a unit vector of an orthonormal basis $\{\boldsymbol{e}_m\}_{m=1,\cdots,dim}$, and $\boldsymbol{g}_m(\boldsymbol{x}'; \boldsymbol{x})$ is the solution of the following time harmonic elastic wave problem defined in the infinite equivalent homogeneous medium submitted to $\delta(\boldsymbol{x} - \boldsymbol{x}')\boldsymbol{e}_m$, a point load at $\boldsymbol{x}'$ oriented in the $\boldsymbol{e}_m$ direction:

$$\boldsymbol{L}^0(\boldsymbol{g}_m(\boldsymbol{x}'; \boldsymbol{x})) + \delta(\boldsymbol{x} - \boldsymbol{x}')\boldsymbol{e}_m = \boldsymbol{0}. \tag{4}$$

To simplify the second term on the right-hand side of equation (2), several assumptions were proposed in [4, 21]. Firstly, the elastic tensor variation and the characteristic function of grains are assumed to vary independently. Secondly, the elastic tensor is assumed to vary independently from grain to grain. Furthermore, by taking into account the single-phase assumption and the fact that the deviation of elastic tensor $\delta \boldsymbol{C}(\boldsymbol{x})$ in each grain, denoted as $\delta \boldsymbol{C}^g$ in the following, is constant, the two-point autocorrelation function of elastic tensors consequently becomes:

$$\langle \delta \boldsymbol{C}(\boldsymbol{x}) \otimes \delta \boldsymbol{C}(\boldsymbol{x}') \rangle = \langle \delta \boldsymbol{C}^g \otimes \delta \boldsymbol{C}^g \rangle W(\boldsymbol{r}) \tag{5}$$

where $W(\boldsymbol{r})$, with $\boldsymbol{r} = \boldsymbol{x} - \boldsymbol{x}'$, denotes the spatial correlation function of two points $\boldsymbol{x}$ and $\boldsymbol{x}'$ describing the possibility that they are in the same grain, and $\langle \delta \boldsymbol{C}^g \otimes \delta \boldsymbol{C}^g \rangle$ the average over all crystallographic orientations [20]. Finally, the problem (2) can be written in the following way:

$$\boldsymbol{L}^0(\langle \boldsymbol{u}(\boldsymbol{x}) \rangle) - \langle \delta \boldsymbol{C}^g \otimes \delta \boldsymbol{C}^g \rangle \overbrace{:}^{(2\cdots 8)\leftarrow} \boldsymbol{Q}(\langle \boldsymbol{u} \rangle; \boldsymbol{x}) = 0 \tag{6}$$

with $\boldsymbol{Q}(\langle \boldsymbol{u} \rangle; \boldsymbol{x})$ a 7-th order tensor defined by:

$$Q_{jklm'n'p'q'}(\langle \boldsymbol{u} \rangle; \boldsymbol{x}) = \frac{\partial}{\partial x_j} \Big(\int_\Omega \frac{\partial G_{m'k}(\boldsymbol{x} - \boldsymbol{x}')}{\partial x_l} \frac{\partial}{\partial x'_{n'}} \big(W(\boldsymbol{x} - \boldsymbol{x}') \frac{\partial \langle u_{p'}(\boldsymbol{x}') \rangle}{\partial x'_{q'}} \big) \, \mathrm{d}\boldsymbol{x}' \Big) \tag{7}$$

In (6), the product operator $\overbrace{:}^{(2\cdots8)\leftarrow}$ indicates that the tensor contraction is applied between the indices from 2 to 8 of the tensor $\langle \delta \boldsymbol{C}^g \otimes \delta \boldsymbol{C}^g \rangle$ and the indices of $\boldsymbol{Q}(\langle \boldsymbol{u} \rangle; \boldsymbol{x})$. Otherwise, the farfield assumption allows replacing $\boldsymbol{G}(\boldsymbol{x}'; \boldsymbol{x})$ by $\boldsymbol{G}(\boldsymbol{0}; \boldsymbol{x} - \boldsymbol{x}') \equiv \boldsymbol{G}(\boldsymbol{x} - \boldsymbol{x}')$.

Now, the basic idea is to find the solution of the problem (6) assuming that it has the form of a plane wave:

$$\langle \boldsymbol{u}(\boldsymbol{x}) \rangle = \boldsymbol{U} e^{ik\hat{\boldsymbol{k}}.\boldsymbol{x}} \tag{8}$$

with $\hat{\boldsymbol{k}}$ a unit vector defining the propagation direction and $\boldsymbol{U}$ the polarization vector. For any angular frequency ω, the propagation constant k is searched under the form $k = \omega/v + i\alpha$ with v the wave velocity and α the attenuation coefficient. The wave scattering due to elastic tensor perturbations can be quantified by analyzing the wave constant k. Indeed, the difference between the real part of k and the real wave constant k_0 in the equivalent homogeneous medium gives the phase velocity deviation from the latter, and its imaginary part quantifies the attenuation.

Putting the plane wave form (8) of the average field solution $\langle \boldsymbol{u}(\boldsymbol{x}) \rangle$ in (6), the following eigenvalue problem of the wave constant k for the perturbed acoustic tensor $\boldsymbol{\Gamma}(k\hat{\boldsymbol{k}})$ can be obtained [4]:

$$\underbrace{\underbrace{\big(\boldsymbol{C}^0 : (\hat{\boldsymbol{k}} \otimes_s \boldsymbol{U})\big).\hat{\boldsymbol{k}}}_{\boldsymbol{\Gamma}^0(\hat{\boldsymbol{k}}).\boldsymbol{U}} - \big(\langle \delta \boldsymbol{C}^g \otimes \delta \boldsymbol{C}^g \rangle \overbrace{:}^{(3\cdots6)\leftarrow} \boldsymbol{P}(k\hat{\boldsymbol{k}})) : (\hat{\boldsymbol{k}} \otimes_s \boldsymbol{U})\big).\hat{\boldsymbol{k}}}_{\boldsymbol{\Gamma}(k\hat{\boldsymbol{k}}).\boldsymbol{U} = \boldsymbol{\Gamma}^0(\hat{\boldsymbol{k}}).\boldsymbol{U} + \delta\boldsymbol{\Gamma}(k\hat{\boldsymbol{k}}).\boldsymbol{U}} = \rho\omega^2 k^{-2} \boldsymbol{U} \tag{9}$$

with:

$$P_{klmn}(k\hat{\boldsymbol{k}}) = \int_{\mathbb{R}^{dim}} G_{km}(\boldsymbol{r}) \frac{\partial^2}{\partial r_n \partial r_l} (W(\boldsymbol{r}) e^{ik\hat{\boldsymbol{k}}.\boldsymbol{r}}) \, \mathrm{d}\boldsymbol{r} \tag{10}$$

We recall that in the equivalent homogeneous medium we have: $\boldsymbol{\Gamma}^0(\hat{\boldsymbol{k}}) \cdot \boldsymbol{U}^0_\beta = \rho\omega^2 k^{-2}_{0\beta} \boldsymbol{U}^0_\beta$ $(\beta = L, T)$, with $\boldsymbol{U}^0_L \parallel \hat{\boldsymbol{k}}$ and $\boldsymbol{U}^0_T \perp \hat{\boldsymbol{k}}$. $k_{0\beta}$ denotes the wave constant in the equivalent homogeneous medium for the longitudinal wave with $\beta = L$ or for the transverse wave with $\beta = T$. A sketch showing in the 3D case the orthonormal basis $\{\boldsymbol{e}_m\}_{m=1,\cdots,3}$, the unit vector of propagation direction $\hat{\boldsymbol{k}}$ and the polarization vectors $\boldsymbol{U}^0_\beta$ is presented in Figure 1.

Otherwise, the expression of the dyadic Green function in an isotropic and homogeneous elastic medium is well known [22, 23]:

$$\boldsymbol{G}(\boldsymbol{r}) = \frac{1}{4\pi\rho\omega^2} \left(\boldsymbol{\nabla}_{\boldsymbol{r}} \big(\boldsymbol{\nabla}_{\boldsymbol{r}} (A(k_{0T} r) - A(k_{0L} r)) \big) + k^2_{0T} A(k_{0T} r) \boldsymbol{I} \right) \tag{11}$$

with $r = |\boldsymbol{r}|$, $\boldsymbol{I}$ the identity tensor, and the function $A(\,\cdot\,)$ is space dimension dependent and is defined by:

$$A^{3D}(k_{0\beta}r) = \frac{e^{ik_{0\beta}r}}{r}\ ,\ A^{2D}(k_{0\beta}r) = i\pi H_0^{(1)}(k_{0\beta}r) \tag{12}$$

In (12), $H_0^{(1)}(\,\cdot\,)$ denotes Hankel function of the first kind. It is worth noticing that, in the case of a 2D problem defined for example in the plane Ox_1x_3, it expresses the outward-propagating cylindrical wave solution, assumed to be uniform along the $\boldsymbol{e}_2$ direction.

The eigenvalue problem (9) is highly nonlinear and its solving is not trivial. However, Stanke and Kino has carried out analytical development of (9) for untextured single-phase polycrystalline media with equiaxed grains in the 3D case (see Eq.(101) and Eq.(102) in [4]). Then they applied the Born approximation to finally obtain explicit formulas for the attenuation coefficient.

Unfortunately, the approach proposed by Stanke and Kino cannot be applied to the 2D case due to Hankel function of the first kind involved in the 2D Green function. To get around this difficulty, our main idea is to assume that, in the case of weakly scattering media, $\boldsymbol{U}$ the wave mode of the average field solution can be approximated by the same type of pure wave mode, *i.e.* $\boldsymbol{U}^0_\beta \parallel \hat{\boldsymbol{k}}$ (for $\beta = L$) or $\boldsymbol{U}^0_\beta \perp \hat{\boldsymbol{k}}$ (for $\beta = T$). Then, by applying the scalar product with $\boldsymbol{U}^0_\beta$ to both side of (9), the following equation for the propagation constant k_β with the wave propagation direction $\hat{\boldsymbol{k}} = \boldsymbol{e}_j$ is obtained:

$$k_\beta^2 - k_{0\beta}^2 = k_\beta^2 \frac{\langle \delta C_{j^\beta jkl} \delta C_{mnj^\beta j} \rangle P_{klmn}(k_\beta \boldsymbol{e}_j)}{C^0_{j^\beta jj^\beta j}} \tag{13}$$

We note that herein the Einstein summation convention is systematically used. In (13), the indice j^β indicates the polarization direction of a β-type wave that propagates in the $\boldsymbol{e}_j$ direction. For example, for $\beta = L$ and $j = 3$, we have $j^\beta = 3$, while for $\beta = T$ and $j = 3$, if the transverse wave is polarized in the space direction $\boldsymbol{e}_1$, we have $j^\beta = 1$.

Now, the use of the Born approximation leads to the assumption that $k_\beta^2 - k_{0\beta}^2 \approx 2k_{0\beta}(k_\beta - k_{0\beta})$ and $k_\beta \approx k_{0\beta}$ on the left and right hand sides of (13), respectively. The following explicit formula is finally established for both 2D and 3D cases:

$$k_\beta = k_{0\beta} + \frac{k_{0\beta}}{2C^0_{j^\beta jj^\beta j}} \langle \delta C_{j^\beta jkl} \delta C_{mnj^\beta j} \rangle P_{klmn}(k_{0\beta} \boldsymbol{e}_j) \tag{14}$$

In the 2D case, even if any analytical derivation of (14) seems impossible due to the complexity of Hankel function, it is very interesting as it can be numerically evaluated by using softwares such as Matlab (see Appendix A1). Hence, both propagation velocity variation and attenuation can then be calculated using

(14). However, in the following, we are only interested in the study of the explicit formula of the attenuation coefficient:

$$\alpha^{\beta} = \mathrm{Im}\big(\frac{k_{0\beta}}{2C^0_{j^\beta jj^\beta j}}\langle\delta C_{j^\beta jkl}\delta C_{mnj^\beta j}\rangle P_{klmn}(k_{0\beta}\boldsymbol{e}_j)\big) \tag{15}$$

where $\mathrm{Im}(\cdot)$ specifies the imaginary part.

Moreover, other interesting explicit formulas can be derived after the calculation of derivatives in the Green function and their decomposition into two parts, $\boldsymbol{G}^{\beta}(\boldsymbol{r})$ (for $\beta = L, T$), related to the longitudinal and transverse waves respectively:

$$\boldsymbol{G}^{\beta}(\boldsymbol{r}) = \frac{(1-c(\beta))}{4\pi\rho\omega^2}(A_{rr}(k_{0\beta}r)\hat{\boldsymbol{r}}\otimes\hat{\boldsymbol{r}} - A_{\boldsymbol{I}}(k_{0\beta}r)\boldsymbol{I}) \tag{16}$$

In (16), $\hat{\boldsymbol{r}}$ denotes the unit vector along the $\boldsymbol{r}$ direction, $c(\beta)$ is a constant equal to 0 for $\beta = L$ and to 2 for $\beta = T$, and the functions A_{rr} and $A_{\boldsymbol{I}}$ are space dimension dependent and are defined by:

$$\begin{aligned}
A^{3D}_{rr}(k_{0\beta}r) &= \frac{e^{ik_{0\beta}r}}{r^3}(3 - 3ik_{0\beta}r - k^2_{0\beta}r^2)\\
A^{3D}_{\boldsymbol{I}}(k_{0\beta}r) &= \frac{e^{ik_{0\beta}r}}{r^3}(1 - ik_{0\beta}r - \frac{c(\beta)}{2}k^2_{0\beta}r^2) \qquad (17a)\\
A^{2D}_{rr}(k_{0\beta}r) &= i\pi(\frac{k_{0\beta}}{r}H^{(1)}_1(k_{0\beta}r) - \frac{1}{2}k^2_{0\beta}(H^{(1)}_0(k_{0\beta}r) - H^{(1)}_2(k_{0\beta}r)))\\
A^{2D}_{\boldsymbol{I}}(k_{0\beta}r) &= i\pi(\frac{k_{0\beta}}{r}H^{(1)}_1(k_{0\beta}r) - \frac{c(\beta)}{2}k^2_{0\beta}H^{(1)}_0(k_{0\beta}r)) \qquad (17b)
\end{aligned}$$

Then, both longitudinal and transverse wave attenuation coefficients, α^L and α^T are expressed as the sum of two terms, one induced by scattering into a same type of wave, and the other generated by mode conversion [10]:

$$\alpha^L = \alpha^{LL} + \alpha^{LT}\ ,\ \alpha^T = \alpha^{TL} + \alpha^{TT} \tag{18}$$

with

$$\alpha^{\beta\gamma} = \mathrm{Im}\big(\frac{k_{0\beta}\langle\delta C_{j^\beta jkl}\delta C_{mnj^\beta j}\rangle}{2C^0_{j^\beta jj^\beta j}}\int_\Omega G^{\gamma}_{km}(\boldsymbol{r})\frac{\partial^2}{\partial r_n\partial r_l}(W(\boldsymbol{r})e^{ik_{0\beta}\boldsymbol{e}_j\cdot\boldsymbol{r}})\,\mathrm{d}\boldsymbol{r}\big) \tag{19}$$

The indices $\beta\gamma = LT, TL$ indicate terms related to wave scattering due to mode conversion between different types of waves at grains boundaries, whereas $\beta\gamma = LL, TT$ indicate terms related to wave scattering due to mode reflection and transmission of a same type of wave at grain boundaries.

We note that the effect of the crystallographic orientation on the attenuation is evaluated, accurately to order of ϵ^2, through the term $\langle\delta C_{j^\beta jkl}\delta C_{mnj^\beta j}\rangle$.

Otherwise, the influence of grain size and shape is measured by the two-point spatial correlation function $W(\boldsymbol{r})$. As there is no further hypotheses imposed to $W(\boldsymbol{r})$, the use of the explicit formulas (15) and (18) is not restricted only to the case of equiaxed grains. Nevertheless, those explicit formulas are valid only in the limit of frequencies below the geometric scattering domain since the Born approximation is made.

It is obvious that the explicit formulas make possible detailed analyses of different involved terms, which is helpful to understand the different scattering mechanisms represented by these terms and to provide an analytical interpretation for the scattering phenomenon in various frequency domains. To do this, the formula (19) of $\alpha^{\beta\gamma}$ is written as the sum of different terms in the following way:

$$\alpha^{\beta\gamma} = \sum_{k,l,m,n} \alpha^{\beta\gamma}_{klmn} \tag{20}$$

with

$$\alpha^{\beta\gamma}_{klmn} \equiv \mathrm{Im}\left(\frac{k_{0\beta}\langle \delta C_{j^\beta jkl}\delta C_{mnj^\beta j}\rangle}{2C^0_{j^\beta jj^\beta j}}\int_\Omega G^\gamma_{km}(\boldsymbol{r})\frac{\partial^2}{\partial r_n \partial r_l}(W(\boldsymbol{r})e^{ik_{0\beta}\boldsymbol{e}_j\cdot\boldsymbol{r}})\,\mathrm{d}\boldsymbol{r}\right) \tag{21}$$

Note that, in (21) the indices k, l, m, and n appearing only once in the left-hand term, their repetition in the right-hand term does not imply summation. It is worth noticing that, due to the symmetries of the elastic tensor and the dyadic Green's tensor, $\alpha^{\beta\gamma}_{klmn}$ shows the following inherent symmetry:

$$\alpha^{\beta\gamma}_{pqqp} = \alpha^{\beta\gamma}_{qppq} \tag{22}$$

Furthermore, it can be shown that the non-zero components are:

$$\langle \delta C_{j^\beta jkl}\delta C_{mnj^\beta j}\rangle \neq 0 \Rightarrow \alpha^{\beta\gamma}_{klmn} \neq 0, \text{ if } \begin{cases} k = l \text{ and } m = n \\ k \neq l \text{ and } mn = kl \text{ or } lk \end{cases} \tag{23}$$

Consequently, there exist only six independent components contributing to $\alpha^{\beta\gamma}$ in the 2D case, while in the 3D case, there are fourteen contributing components for each set of α^{LL} and α^{LT}, and fifteen contributing components for each set of α^{TT} and α^{TL}. We note that, in the 2D case under the plane strain assumption, the elastic constants associated with $\boldsymbol{e}_2$ direction are not involved.

It is worth noticing that the explicit formulas developed in the present work can be applied to polycrystalline materials containing crystallites of any symmetry class, provided that the average correlation functions of elastic tensor $\langle \delta\boldsymbol{C}^g \otimes \delta\boldsymbol{C}^g\rangle$ are calculated [24]. In the following, the β-titanium metal is taken as an example for analytical calculations. The choice is dictated by the increasing interest for titanium alloys due to their superior combination of properties. Final parts are frequently obtained by hot forming so that ultrasonic investigation is a suitable tool to follow microstructure evolutions during the process.

For the β-titanium, its inhomogeneity degrees ϵ_β, defined in [4] with respect to the wave propagation constants, ranks between the aluminum low anisotropy [4] and the higher anisotropy of Inconel 600 [25]. Though the influence of the inhomogeneity degrees on the attenuation coefficient is beyond the scope of this work, a comparison is presented in Appendix A2 between three different materials, which confirms that the results obtained for β-titanium are valid and could be extended. The attenuation coefficients α, $\alpha^{\beta\gamma}$ and their different non-zero contributing terms $\alpha^{\beta\gamma}_{klmn}$ have been calculated, in order to highlight some common and different features between 2D and 3D scattering phenomena.

3. Main common and different features between 2D and 3D attenuation phenomena

The material properties of the considered β-titanium polycrystalline material are given in Table I. Its degree of anisotropy for longitudinal waves, $\epsilon_L = 2.74\%$, is twice larger than the one of aluminum but still very low compared to unity [4] and its average correlation functions of elastic tensor $\langle \delta C_{j^\beta jkl} \delta C_{mnj^\beta j} \rangle$ are given by Table 2 in [26]. Due to the equiaxed grain assumption, $W(\boldsymbol{r}) = W(r)$ depends only on the scalar variable r. In the present work, as often proposed in the relative literature [27], $W(r)$ is approximated by an exponential function $W(r) = e^{-2r/d}$, with d the grain size.

	C_{1111} (GPa)	C_{1122} (GPa)	C_{2323} (GPa)	$\epsilon_L(\%)$	$\epsilon_T(\%)$	ρ (kg/m^3)
Single Crystallite in cubic axes	134.0	110.0	36.0	2.74	8.73	4428
Equivalent homogeneous medium	153.0	100.0	26.5	0.0	0.0	4428

Table I: Elastic properties of a BCC β-titanium metal [28].

In the following, as usually done to obtain a master curve for attenuation vs. frequency, which is independent on the grain size, αd the attenuation per crystallite is drawn with respect to $x_{0\beta}$ the normalized frequency using the base-10 logarithmic scale. $x_{0\beta} = 2\pi d/\lambda_\beta = 2\pi f d/v_{0\beta}$ is the ratio of the grain size d to the wavelength λ_β, with $v_{0\beta}$ the wave velocity in the equivalent homogeneous medium.

First of all, the explicit formula of the attenuation (15) is validated for longitudinal waves in the 3D case by comparison with the model of Stanke and Kino. Figure 2 shows that the explicit formula (15) slightly underestimates the attenuation compared to the Stank-Kino's model and the relative difference in attenuation coefficient between both models is less than 0.8%. Therefore, we

can use the proposed explicit formulas to get further analytical comparisons between the 2D and 3D cases.

3.1. Asymptotic and the transition behaviors of Rayleigh and stochastic regions

It has been shown, in the preceding section, that the scattering-induced attenuation results from wave mode conversion and wave mode reflection/transmission, which can be measured by $\alpha^{\beta\gamma}$ with $\beta \neq \gamma$ and $\alpha^{\beta\beta}$ respectively. Originally proposed in 3D within the framework of the Weaver's model [13], these two mechanisms are highlighted within the framework of the Stanke and Kino's model in 3D and extended in 2D in the present work. A particular attention is therefore paid to the behavior of the $\beta\gamma$ and $\beta\beta$ attenuation components in the 2D case and compared to the 3D case within the different scattering regions.

Both cases of longitudinal and transverse waves are considered and the corresponding master curves of attenuation per crystallite coefficient, $\log_{10}(\alpha d)$ vs. $\log_{10}(x_0)$, are presented in Figures 3(a) and (b), respectively. Otherwise, to better quantify comparisons between the 2D and 3D cases, curves of the ratio $\alpha^{\beta,3D}/\alpha^{\beta,2D}$ and of the slope of the master curves are also plotted and analyzed (Figure 4). We recall that the limits between the Rayleigh and stochastic regions cannot be strictly pinpointed. In Figures 3 and 4, the Rayleigh region is asymptotically located in the lowest frequency range, corresponding to the smallest values of $x_{0\beta}$, while the stochastic one corresponds to the high frequency range and the large $x_{0\beta}$ values. The 2D and 3D cases are to be compared in the following, including for the scattering mechanisms in the Rayleigh and the stochastic regions, the slope variations of the master curves, the frequency dependence of attenuation in different regions and the attenuation levels.

Concerning the scattering mechanism in the stochastic region, a same behavior is observed whatever the propagating wave type and whatever the space dimension: the scattering is mainly controlled by the reflection/transmission of the same type of wave mode. For example, α^{LL} the attenuation due to longitudinal-to-longitudinal wave scattering contributes to more than 94% of the total attenuation for $(x_{0L}, \log_{10} x_{0L}) = (31.6, 1.5)$, which corresponds to the upper range of the stochastic region (Figure 3(a)). The contribution of α^{LT} or α^{TL} the attenuation due to wave mode conversion is mush less significant (by two or three orders of magnitude).

But, in the Rayleigh region, the scattering phenomenon differs between longitudinal and transverse waves:

- For the longitudinal waves, the scattering mechanism is governed by the conversion between longitudinal and transverse wave modes. For example, α^{LT} the attenuation due to longitudinal-to-transverse wave scattering makes a contribution of more than 96% to the total attenuation for

$(x_{0L}, \log_{10} x_{0L}) = (0.08, -1.1)$ (Figure 3(a)). The attenuation α^{LT} due to the wave mode conversion is higher by almost two orders of magnitude than α^{LL}. However, when frequencies increase, this contribution decreases and becomes independent on frequency beyond $(x_{0L}, \log_{10} x_{0L}) \approx (4.2, 0.6)$, due to the transition from Rayleigh to stochastic regions.

- For the transverse waves, conversely, the attenuation α^{TT} due to transverse-to-transverse scattering is at least two orders of magnitude higher than α^{TL} coming from the wave mode conversion (Figure 3(b)).

As a consequence, it can be noticed that, the transition between the Rayleigh region and the stochastic one is different between the two cases of longitudinal and transverse waves. It is due to the fact that a same scattering mechanism is active whatever the frequency region in the case of the transverse waves, while two different scattering mechanisms are active depending on the involved frequency domain in the case of longitudinal waves. Accordingly, in the case of transverse waves, a monotonically decreasing slope of the master $\log_{10}(\alpha d)$ vs. $\log_{10}(x_0)$ curves is observed (right axis of Figure 4(b)). While, in the case of longitudinal waves, an inflection point exists for the master curve and indicates the Rayleigh-to-stochastic transition (right axis of Figure 4(a)). Moreover, it is reasonable to state that the transition starts at lower frequencies in the 2D case than in the 3D case, according to the inflection points obtained in both cases shown in Figure 4(a).

Comparison in the frequency dependence of the attenuation per crystallite coefficient, i.e. the exponent n value, between 2D and 3D cases is further made based on the slope of the master curves. Previous studies in the 3D case suggested that the scattering-induced attenuation per crystallite coefficient αd was proportional to $x_{0\beta}^n$, with a specific asymptotic value of the exponent n dependent on the scattering region: $n = 4$ in the Rayleigh region and $n = 2$ in the stochastic region [4]. In the 2D case, Figures 4(a) and (b) (right axis in blue) show a different frequency dependence of the attenuation per crystallite in the Rayleigh region: $n = 3$ for the both cases of longitudinal and transverse waves. This result confirms the classic argument already obtained in the 3D case [4, 13] that the Rayleigh scattering region is dependent on the volume of grain as in the 2D case the grain volume is reduced to its surface. On the other hand, the exponent n is equal to 2 in the stochastic region for both 2D and 3D cases. However, the evolution of the exponent n from the Rayleigh region to the stochastic one differs between the two cases of longitudinal and transverse waves: for the longitudinal waves, the exponent decreases at first, then increases and tends to 2, while for the transverse waves, it decreases continuously tends to 2 for the 3D case and to a value very close to 2 in the 2D case.

As far as the comparison in the attenuation level between 2D and 3D is concerned, the attenuation differs mostly in the Rayleigh region for both longitudinal and transverse waves: the attenuation coefficient obtained in the 3D

case is about one order of magnitude less than the one obtained in the 2D case. The difference between the 2D and 3D attenuation values decrease as the frequency increases. But, such difference is inverted within or after the Rayleigh-to-stochastic transition domain: the 3D attenuation coefficient becomes larger than the 2D one. For example, in the case of longitudinal waves a maximum ratio $\alpha^{L,3D}/\alpha^{L,2D}$ equal to 1.75 is obtained, which occurs within the Rayleigh-to-stochastic transition domain and is dependent on the inhomogeneity degree ϵ of the material (left axis of Figure 4(a)). In the case of transverse waves, the ratio $\alpha^{T,3D}/\alpha^{T,2D}$ is an monotonic increasing function, which tends towards 1.5 in the stochastic region (left axis of Figure 4(b)).

3.2. Analytical interpretation of dominant scattering mechanisms

Now, the non-zero components of the attenuation coefficient $\alpha^{\beta\gamma}_{klmn}$ defined in Section 2, which describe scattering contributions at grain boundary into all directions, are separately presented and analyzed. The propagation direction is taken to be the $\boldsymbol{e}_3$ direction, *i.e.* $j = 3$ in (15) and (19), without loss of generality. We note that in the 3D case the assumption of macroscopically untextured media leads to an equivalence of the directions $\boldsymbol{e}_1$ and $\boldsymbol{e}_2$ with respect to the propagation direction $\boldsymbol{e}_3$. This implies more particularly for the longitudinal waves that there is equality between some corresponding components $\alpha^{\beta\gamma}_{klmn}$, e.g. $\alpha^{LT}_{1313} = \alpha^{LT}_{2323}$.

The case of longitudinal waves is firstly analyzed.

- In the stochastic scattering region, which corresponds to the frequency range $x_{0L} \in]5, 35[$ for the considered polycrystals, it has been shown that α^{LL} due to L-wave mode reflection/transmission is predominant. All the non-zero components α^{LL}_{klmn} are plotted in Figure 5 and among them, it is obvious that α^{LL}_{3333} makes the dominant contribution to α^{LL}. Detailed analysis of the equations given in Section 2, *e.g.* (2), (3), (19) and (20), show that among the different components contributing to α^{LL}, only α^{LL}_{3333} is due to a "pure" L-wave mode reflection/transmission in the sense that it involves only longitudinal wave modes propagating and polarized in the $\boldsymbol{e}_3$ direction. Therefore, this result is in agreement with the fact that the stochastic scattering can be regarded as a one-dimensional phenomenon linked to only the averaged grain length along the wave propagation direction. This analysis of the components of α^{LL} provides an analytical interpretation for first power dependence of attenuation on grain size and a similar attenuation level in the stochastic domain for longitudinal waves for both the 2D and 3D models.

- In the Rayleigh scattering region that corresponds to the frequency range $x_{0L} \in]0, 0.6[$ for the considered polycrystals, it has been shown that α^{LT} due to wave mode conversion is predominant. Indeed, as can be seen from

Figure 3, α^{LT} increases and gradually becomes insensitive to frequency, making a negligible contribution in the stochastic scattering region. All the non-zero components α^{LT}_{klmn} are therefore plotted only in the Rayleigh scattering in Figure 6 and it is obvious that their contributions to α^{LT} are comparable. In other words, it is important to take into account all possible mechanisms. Taking the 2D case as an example, the longitudinal wave mode propagating and polarized in the $\boldsymbol{e}_3$ direction can, due to $\delta\boldsymbol{C}$, result in a mode (stress vector) propagating in the $\boldsymbol{e}_n$ direction and polarized in the $\boldsymbol{e}_m$ direction. It gives rise to a mode propagating in the $\boldsymbol{e}_l$ direction and polarized in the $\boldsymbol{e}_k$ direction, which finally contributes to a transverse wave mode. This result confirms that the Rayleigh scattering involves all space directions and provides an analytical interpretation of its dependency on the grain volume (or surface) in the 3D (or 2D) case. However, we note that, for example in the 2D case, the two most important contributions are given by α^{LT}_{1313} and α^{LT}_{3131}.

- Another interesting result is that all the components α^{LT}_{nmmn} with $m \neq n$ are negative, which correspond to an amplification instead of an attenuation. Detailed analysis of such components shows that it results from the partial derivative term $\partial^2/\partial r_n \partial r_m (W(r) e^{ik_{0L}\boldsymbol{e}_3 \cdot \boldsymbol{r}})$ which works out to be negative when $m \neq n$. However, this cannot explain completely why α^{LT}_{nmmn} is negative. Indeed, according to the definition of the tensor $\boldsymbol{P}$ (10), when $m \neq n$, the negative partial derivative term leads to $P_{nmmn} < 0$ and $P_{mmnn} < 0$. But, because of the fact that, $\langle \delta C_{33mn} \delta C_{nm33} \rangle > 0$, and $\langle \delta C_{33mm} \delta C_{nn33} \rangle < 0$ when $m \neq n$ [26], only α^{LT}_{nmmn} is negative. One plausible interpretation is α^{LT}_{nmmn} (or α^{LT}_{mmnn}) expresses an intermediate mode conversion between two modes, one propagating in the $\boldsymbol{e}_n$ direction and polarized in the $\boldsymbol{e}_m$ (or $\boldsymbol{e}_n$) direction and the other propagating in the $\boldsymbol{e}_m$ direction and polarized in the $\boldsymbol{e}_n$ (or $\boldsymbol{e}_m$) direction. Therefore, when the correlation between the corresponding elastic constants is positive in the case with $n \neq m$, the attenuation in the $\boldsymbol{e}_n$ direction gives rise to an amplification in the perpendicular $\boldsymbol{e}_m$ direction.

Then, the case of transverse waves is analyzed. It has been shown that α^{TT} due to T-wave mode reflection/transmission is predominant in both the Rayleigh and the stochastic scattering regions. All the non-zero components α^{TT}_{klmn} are plotted in Figure 7, with an enlarged view at low frequencies in the Rayleigh region $x_{0T} \in]0.2, 0.6[$. Analyses similar to the case of longitudinal waves are obtained.

- In the Rayleigh region, each component makes a comparable contribution to α^{TT}, which confirms that the Rayleigh scattering involves all space directions and provides an analytical interpretation of its dependency on the grain volume (or surface) in the 3D (or 2D) case.
- In the stochastic region, only the component α^{TT}_{1313} in the 2D case and

only the components α^{TT}_{1313} and α^{TT}_{2323} in the 3D case make significant contributions. More particularly, the contribution of α^{TT}_{1313} is dominant and expresses, according to the analysis presented above, a "pure" T-wave mode reflection/transmission involving only transverse wave modes propagating in the $\boldsymbol{e}_3$ direction and polarized in the $\boldsymbol{e}_1$ direction. Once again, the stochastic scattering for transverse waves can be considered as a one-dimension phenomenon depending only on the average grain length in the propagation direction. Otherwise, in the 3D case, α^{TT}_{2323} gives also an important contribution. However, quantitative comparison shows a comparable magnitude of α^{TT}_{1313} between the 2D and 3D cases, so the contribution in the 3D case of α^{TT}_{2323}, *i.e.* the third direction $\boldsymbol{e}_2$ ignored by 2D models, leads to $\alpha^{T,3D} > \alpha^{T,2D}$ in the stochastic region, with the ratio $\alpha^{T,3D}/\alpha^{T,2D}$ tends to a value larger than 1.5 (Figure 4(b)).

From above discussions, main common and different features between both 2D and 3D cases of the grain scattering induced attenuation are analyzed, such as a decrease in the frequency and grain size dependence and an increase in the attenuation levels in the Rayleigh region for both longitudinal and transverse waves propagating within a 2D polycrystal medium. However, in essence, the scattering mechanisms are the same in 2D and 3D cases, i.e., the Rayleigh scattering is dependent on the volume of grains, while the stochastic scattering is dependent only on the grain length along the wave propagation direction. From this point of view, the attenuation in an infinite 3D space can be deduced according to more efficient 2D simulations given that the Born approximation is valid.

4. Numerical validation and analysis

4.1. Computational model

To study the effect of the grain size on the grain scattering-induced attenuation, 2D FE simulations were performed using an in-house software OOFE (Object Oriented Finite Element program) [29]. It is an implicit solver based on a time-discontinuous space-time Galerkin method [30, 31]. The details of the FE modeling, such as the use of structured and unstructured meshes, comparison of symmetry and periodic boundary conditions, and the mesh convergence, have been described elsewhere [15, 16, 20, 25, 32, 33]. Here, only the necessary steps to numerically model a plane wave propagation within an anisotropic heterogeneous polycrystalline medium are discussed. The same material is taken as for the analytical calculation.

A polycrystalline medium is generated by a Voronoï tessellation, as achieved for example in [15, 32, 34–38], which has been shown to represent closely a realistic polycrystalline microstructure. Three different mean grain sizes were

considered: 34, 80, and 160μm. We chose a rectangular sample of dimension $W \times H$ (x-coordinates $\times$ y-coordinates) (Figure 8), with $H = 10.16$mm. For the two largest grain sizes, $W = 20.32$mm, while $W = 5.08$mm for the smallest grain size of 34μm to reduce the memory required for the calculation. Details of FE model are depicted in Table II. The grain diameter follows a Gaussian distribution with a constant standard deviation equal to about 0.1 whatever the grain size. To obtain an untextured polycrystal, crystallographic orientation for each grain defined by the Euler angle $\theta(\varphi_1, \phi, \varphi_2)$, which gives the orientation of the cubic axes of each grain with respect to the specimen Cartesian basis, is randomly chosen: $\varphi_1 = \text{random}[0, 2\pi[$, $\phi = \arccos(\text{random}[-1, 1])$ and $\varphi_2 = \text{random}[0, 2\pi[$.

Mean grain size D	34μm	80μm	160μm
Center frequencies	4-16MHz	4-16MHz	4-16MHz
Dimension(mm) $(W \times H)$	5.08×10.16	20.32×10.16	20.32×10.16
Grains in each sample	53656	38758	11427
No. of samples	5	7	23

Table II: Details of numerical FE model.

Discretization size used both in the time and space is of great importance for the accuracy of the numerical results. For numerical simulation of wave propagation in homogeneous media, it is generally recommended to have at least 15 elements included in the shortest wavelength of interest. However, in polycrystalline media, denser elements are required when the grain size is of an order of magnitude much smaller than the shortest wavelength [15, 18, 20, 39]. Investigations indicate that numerical calculations of ultrasonic attenuation and/or scattering converge at a smaller d/h value for a sample with a smaller grain size [15, 20, 39]. In the present work, the ratio of grain size to element size, d/h, has been set to be approximately 6.0 for samples with the grain sizes of 34 and 80μm, and to be around 12.0 for the grain size of 160μm, which corresponds to more than 30 elements per shortest wavelength. The calculation of the attenuation coefficient converges for an acceptable threshold of 5.5% for all the considered grain sizes. Once the element size is defined, the accuracy of time integration of the implicit solver is guaranteed given that the time step Δt is no more than the smallest transit time of the wave through any of the elements: $\Delta t \leq h_{min}/\max_\theta(v_L)$, where h_{min} is the smallest element size [18].

For simulating a scenario of a longitudinal plane wave in an infinite domain as assumed in the analytical model, a uniformly distributed pressure loading $p(\boldsymbol{x}, t)\boldsymbol{e}_y$ is imposed to all the nodes on the emitter line, in this case the $y = Y0$ line in Figure 8, with $\boldsymbol{e}_y$ denoting the unit vector in the y direction. To simulate a broadband ultrasonic incident signal representing an ablative laser pulse, the amplitude of the pressure loading is the sum of two Ricker signals varying in time, whose frequency content is centered to 5MHz and 10MHz respectively.

For such an external loading, the valid frequency domain is limited to a range from 4 to 16MHz, this leads to a range from 375μm to 1.5mm for wavelengths. Hence, the Rayleigh region and the Rayleigh-to-stochastic transition domain are covered with respect to the considered grain sizes. Symmetry boundary condition is used to accommodate the desired plane wave mode, *i.e.*, vanishing nodal displacements (and thus also velocities and accelerations) in the direction normal to the two lines that are parallel to the wave propagation direction, namely $x = X0$ and $x = X1$ in Figure 8. The displacement and velocity of all the nodes on the emitter line $y = Y0$ and the receiver line $y = Y1$ are recorded.

To reduce the gap between the numerical simulation involving a finite number of grains and the analytical models, multiple realizations of microstructures with randomly generated crystallographic orientations but with the same Voronoï-type grain morphology are calculated. The number of realizations is set to be 5, 7 and 23 for the three grain sizes of 34, 80 and 160μm, respectively, resulting in roughly the same number of grains considered for each grain size. The attenuation for each grain size is then calculated by averaging over the corresponding realizations.

4.2. Numerical results and comparison with the theoretical model

The averaged numerical results (represented as solid circles) and the minimum and maximum limits (represented as bars) of attenuation are plotted as a function of frequency in Figure 9. In the low frequency region $[4, 13]$MHz, the attenuation coefficient increases continuously as frequency for a given grain size, and increases as grain size at a given frequency. By contrast, in the higher frequency region $[12, 16]$MHz, a similar evolution tendency is observed only for samples with both grain sizes of 34 and 80μm. Indeed, by comparing the grain size to the wavelength in this frequency region, the Rayleigh scattering behavior is mainly found for the two smallest grain sizes, whereas the Rayleigh-to-stochastic scattering transition behavior is found for the largest grain size of 160μm, which reduces greatly the power dependence of attenuation on frequency. However, the results for the largest grain size of 160 μm is shown to be non-monotonic in the high frequency region $[15, 16]$MHz, which is not expected by the classical Stanke-Kino theory considering only one single mean grain size. It can be probably attributed to the distribution of grain sizes [25] and will be discussed in the end of this section.

Figure 10(a) presents, using the base-10 logarithmic scale and for the 2D case, master curves, calculated analytically and numerically, of αd the attenuation coefficient per crystallite versus x_0 the normalized frequency. The FE calculations for the three different grain sizes are well superimposed on the analytical master curve. The reduction of frequency dependence of attenuation in the Rayleigh region, from the exponent $n = 4$ for the 3D case to $n = 3$ for the 2D case, is quantitatively confirmed for frequency range $(x_{0L}, \log_{10} x_{0L}) <$

$(0.6, -0.22)$ by the numerical results. Afterwards, for the Rayleigh-to-stochastic transition, the first concave hump is roughly recovered for frequencies $x_0 > 0.6$ by the numerical results. Nevertheless, rigorous comparison shows that the numerically estimated transition region is more pronounced than the analytically predicted one. Specifically, the attenuation level becomes slightly larger in the region $0.6 < x_0 < 2.4$ (corresponding to $-0.22 < \log_{10}(x_{0L}) < 0.38$).

As discussed in Section 2, the inverse exponential two-point correlation function under the assumption of Poisson-distributed cord length is used for the feasibility of the analytical deviation. However, a series of studies have proved that this form of correlation function failed to consider effects of a complete grain-size distribution on ultrasonic attenuation [14, 25, 33]. In the FE modeling presented here, a relative small distribution width of grain sizes was generated, which would give rise to a strong deviation of the spatial correlation function model from the exponential form, and accordingly lead to the disagreement between the classical analytical model and our numerical models. It has been demonstrated [25], that the attenuation behavior in the transition region strongly depends on the grain morphology and grain size distribution, as it is dominated by the mode conversion component α^{LT}.

Thanks to $\alpha^{L,3D}/\alpha^{L,2D}$ (Eq. 15) the analytically identified ratio of attenuation coefficient between 3D and 2D models, 3D estimations can be deduced by 2D simulations. Comparison between the deduced 3D results for different grain sizes and the analytical prediction is plotted in Figure 10(b), which shows an acceptable agreement. It is demonstrated that more efficient 2D simulations can be conducted to be representative for the 3D case on condition that the Born approximation is valid.

5. Conclusions

In this paper, the grain scattering-induced attenuation coefficient has been expressed in an explicit integral form of the dyadic Green's tensor and a spatial correlation function, applicable for ultrasonic waves propagating in both 2D and 3D polycrystalline media. Especially, the explicit formula in 2D allowed the Stanke and Kino's master curve of the effect of grain size on attenuation to be drawn and compared with the 3D original.

Several different and common features for the 2D and 3D attenuation phenomena were observed and discussed. In the Rayleigh region, the attenuation of the 2D model shows a reduction of the frequency and grain size dependence, which results in a higher attenuation level compared to the 3D model. Conversely, in the stochastic region, a same frequency and grain size dependence is obtained for both 2D and 3D cases. As far as the attenuation level is concerned within or after the Rayleigh-to-stochastic transition domain, the difference be-

tween the 2D and 3D cases is inverted. For the longitudinal waves, the attenuation in 3D becomes higher than in 2D and the ratio of attenuation between the two cases reaches a maximum value (equal to 1.75 for the studied polycrystal) within the Rayleigh-to-stochastic transition domain, then it decreases and tends to the value of 1. For the transverse waves, the ratio of attenuation between the 3D and 2D cases is an monotonic increasing function of frequency from the Rayleigh region to the stochastic region (which tends to the value of 1.5 for the studied polycrystal).

Two levels of decomposition of the attenuation coefficient in different scattering-induced coefficients were proposed and allowed a better understanding of the scattering mechanisms leading to wave attenuation in a polycrystal. For the stochastic region, the dominating scattering mechanism is the reflection / transmission between a same type of wave modes, whatever the space dimension and the type of waves. Detailed analysis, owing to the second level of decomposition of the mode reflection / transmission contribution, provided an analytical interpretation of the fact that the attenuation is only controlled by the averaged grain length along the wave propagation direction. It gave also an explanation for a higher attenuation coefficient of the transverse wave in 3D than in 2D in the stochastic region. For the Rayleigh region, the dominating scattering mechanism differs between the longitudinal waves and the transverse ones, which is the longitudinal/transverse conversion for the longitudinal waves and the transverse-to-transverse reflection/transmission for the transverses waves. However, detailed analysis based on the second level of decomposition allowed a good explanation of the fact that attenuation in Rayleigh region mainly depends on the grain volume.

2D FE simulations were performed in an untextured body-centered-cubic (bcc) titanium polycrystal with equiaxed grains. A Voronoï-type grain microstructure with a narrow Gaussian distribution of sizes was studied. Several average grain sizes were considered and they were chosen to cover the Rayleigh and the Rayleigh-to-stochastic transition regions. A good agreement was found in the Rayleigh region between the numerical simulations and the analytical predictions which validates the FE modeling. Nevertheless, an oscillatory behavior was found in the transition region due to the influence of grain size distribution, which was not considered by the exponential form of spatial correlation function used in the analytical deviation. 3D numerical estimations were deduced from 2D FE simulations thanks to the ratio of analytical attenuation coefficient between the 3D and the 2D modelings. These results are expected to be useful for achieving efficient 2D simulations that could be representative of 3D.

Acknowledgments

The authors wish to thank the French National Center for Scientific Research (CNRS), CentraleSupélec and the China Scholarship Council (CSC) for their financial supports of this research work. Computations were performed using HPC resources from the computing centre of CentraleSupelec and ENS Paris-Saclay. The later period of this work was also financially supported by the National Natural Science Foundation of China (Project No. 51805304).

Appendix A1. Numerical calculation of the explicit formulas of the attenuation coefficients

Detailed equations and numerical procedure developed to evaluate the attenuation coefficients defined by (18) are hereafter presented.

Given the material properties, a mean grain size d and the normalized frequency region of interest, the objective is to calculate all the contributing terms $\alpha_{klmn}^{\beta\gamma}$ $(\beta,\gamma = L,T)$, which are mainly defined using two second order symmetric tensors $\boldsymbol{G}^{\beta}(\boldsymbol{r})$ and $\boldsymbol{D}^{\beta}(\boldsymbol{r})$. The Green function tensor $\boldsymbol{G}^{\beta}(\boldsymbol{r})$ is given by (16). Otherwise, assuming that the ultrasonic wave propagates in the $\boldsymbol{e}_3$ direction and the spatial correlation function has an inverse exponential form $W(\boldsymbol{r}) = e^{-r/a}$, with $a = d/2$, it can be shown that the second derivative tensor $\boldsymbol{D}^{\beta}(\boldsymbol{r})$ reads as:

$$\begin{aligned}\boldsymbol{D}^{\beta}(\boldsymbol{r}) &\equiv \boldsymbol{\nabla}_{\boldsymbol{r}}(\boldsymbol{\nabla}_{\boldsymbol{r}}(W(\boldsymbol{r})e^{ik_{0\beta}\boldsymbol{e}_3\cdot\boldsymbol{r}}) \\ &= e^{ik_{0\beta}r\boldsymbol{e}_3\cdot\hat{\boldsymbol{r}}-r/a}\big((\frac{1}{ra}+\frac{1}{a^2})\hat{\boldsymbol{r}}\otimes\hat{\boldsymbol{r}}-\frac{1}{ra}\boldsymbol{I}-k_{0\beta}^2\boldsymbol{e}_3\otimes\boldsymbol{e}_3-\frac{2ik_{0\beta}}{a}\hat{\boldsymbol{r}}\otimes_s\boldsymbol{e_3}\big)\end{aligned} \tag{24}$$

with $\hat{\boldsymbol{r}}$ the unit vector defining the direction of $\boldsymbol{r}$.

For convenience of calculation, the Cartesian coordinates (r_1, r_3) for the 2D case (resp. (r_1, r_2, r_3) for the 3D case) are converted into the polar coordinates (r,θ) (resp. the spherical coordinate (r,θ,φ)). Then, the equation (19) to be calculated finally becomes:

$$\alpha^{\beta\gamma,2D} = \mathrm{Im}\left(\frac{k_{0\beta}\langle\delta C_{j^\beta jkl}\delta C_{mnj^\beta j}\rangle}{2C^0_{j^\beta jj^\beta j}}\int_{r=0}^{\infty}\int_{\theta=0}^{2\pi}G^{\gamma}_{km}(r,\theta)D^{\beta}_{ln}(r,\theta)r\,\mathrm{d}\theta\,\mathrm{d}r\right) \tag{25a}$$

$$\alpha^{\beta\gamma,3D} = \mathrm{Im}\left(\frac{k_{0\beta}\langle\delta C_{j^\beta jkl}\delta C_{mnj^\beta j}\rangle}{2C^0_{j^\beta jj^\beta j}}\int_{r=0}^{\infty}\int_{\varphi=0}^{\pi}\int_{\theta=0}^{2\pi}G^{\gamma}_{km}(r,\theta,\varphi)D^{\beta}_{ln}(r,\theta,\varphi)r^2\sin\varphi\,\mathrm{d}\theta\,\mathrm{d}\varphi\,\mathrm{d}r\right) \tag{25b}$$

In (25), the two-points autocorrelation function of elastic constants $\langle \delta C_{j^\beta jkl} \delta C_{mnj^\beta j} \rangle$ are given by Eq.(100) in [4]. Taking an overall consideration of the symmetry properties of the tensors $\delta \boldsymbol{C}$, $\boldsymbol{G}(\boldsymbol{r})$ and $\boldsymbol{D}(\boldsymbol{r})$, it is found that only six components $\alpha^{\beta\gamma}_{klmn}$ have to be calculated in the 2D case, while in the 3D case, there are fourteen components to calculate for α^{LL} and α^{LT} and fifteen for α^{TT}.

Two integration methods are developed and compared.

The first method calculate numerically the double and triple integrals defined by (25). In this case, MATLAB functions "integral2" and "integral3" are used. In order to guarantee the precision of numerical integration and to determine a pertinent interval of integration for the variable $r \in [0, \infty]$, the variation of the integrands defined in (25) within the infinite interval $[0, \infty]$ of the variable r is analyzed. Figure 11 illustrates the variation in the 2D case. Given values of θ and x_0, the integrands decrease very rapidly in the region $r \ll d$ and become very close to zero when $r \gg d$. According to this analysis, the interval of integration for r is chosen equal to $[0.0001d, 100d]$, which is furthermore subdivided into five subintervals: $[0.0001d, 0.1d] \cup [0.1d, 0.25d] \cup [0.25d, d] \cup [d, 10d] \cup [10d, 100d]$. In each subinterval, the MATLAB 2D or 3D integral functions are applied with the default relative and absolute error tolerances. We remark that this method applied to the 3D explicit formula is very time consuming and to speed up the calculation in higher frequency region, it is possible to relax both relative and absolute error tolerances.

The second method calculates firstly and analytically all the integrals with respect to θ in the 2D case (resp. to (θ, φ) in the 3D case). Then the integrals with respect to r are performed numerically, using for exemple MATLAB function "integral".

In the 2D case, after the analytical development of the integrals with respect to θ, the ~~six~~five integrands $\eta^{\beta\gamma}_{kmln}$ useful for the calculation of $\alpha^{\beta\gamma}_{klmn}$, without

the part $\frac{\langle \delta C_{j^\beta jkl} \delta C_{mnj^\beta j} \rangle}{2C^0_{j^\beta jj^\beta j}} \frac{(1-c(\gamma))}{4\pi\rho\omega^2}$, can be expressed as follows:

$$
\begin{aligned}
\frac{\eta^{\beta\gamma}_{3333}(r)}{k_{0\beta}re^{-r/a}} =& A_{rr}(k_{0\gamma}r)\big((\frac{1}{ra}+\frac{1}{a^2})\hbar^{2D}_{C4}(k_{0\beta}r) - \frac{2ik_{0\beta}}{a}\hbar^{2D}_{C3}(k_{0\beta}r) - (k^2_{0\beta}+\frac{1}{ra})\hbar^{2D}_{C2}(k_{0\beta}r)\big) \\
& - A_{\boldsymbol{I}}(k_{0\gamma}r)\big((\frac{1}{ra}+\frac{1}{a^2})\hbar^{2D}_{C2}(k_{0\beta}r) - \frac{2ik_{0\beta}}{a}\hbar^{2D}_{C1}(k_{0\beta}r) - (k^2_{0\beta}+\frac{1}{ra})\hbar^{2D}_{S0}(k_{0\beta}r)\big) \\
\frac{\eta^{\beta\gamma}_{1111}(r)}{k_{0\beta}re^{-r/a}} =& A_{rr}(k_{0\gamma}r)\big((\frac{1}{ra}+\frac{1}{a^2})\hbar^{2D}_{S4}(k_{0\beta}r) - \frac{1}{ra}\hbar^{2D}_{S2}(k_{0\beta}r)\big) \\
& - A_{\boldsymbol{I}}(k_{0\gamma}r)\big((\frac{1}{ra}+\frac{1}{a^2})\hbar^{2D}_{S2}(k_{0\beta}r) - \frac{1}{ra}\hbar^{2D}_{S0}(k_{0\beta}r)\big) \\
\frac{\eta^{\beta\gamma}_{1313}(r)}{k_{0\beta}re^{-r/a}} =& A_{rr}(k_{0\gamma}r)\big((\frac{1}{ra}+\frac{1}{a^2})\hbar^{2D}_{S2C2}(k_{0\beta}r) - \frac{ik_{0\beta}}{a}\hbar^{2D}_{S2C1}(k_{0\beta}r)\big) \\
\frac{\eta^{\beta\gamma}_{1133}(r)}{k_{0\beta}re^{-r/a}} =& A_{rr}(k_{0\gamma}r)\big((\frac{1}{ra}+\frac{1}{a^2})\hbar^{2D}_{S2C2}(k_{0\beta}r) - \frac{2ik_{0\beta}}{a}\hbar^{2D}_{S2C1}(k_{0\beta}r) - (k^2_{0\beta}+\frac{1}{ra})\hbar^{2D}_{S2}(k_{0\beta}r)\big) \\
& - A_{\boldsymbol{I}}(k_{0\gamma}r)\big((\frac{1}{ra}+\frac{1}{a^2})\hbar^{2D}_{C2}(k_{0\beta}r) - \frac{2ik_{0\beta}}{a}\hbar^{2D}_{C1}(k_{0\beta}r) - (k^2_{0\beta}+\frac{1}{ra})\hbar^{2D}_{S0}(k_{0\beta}r)\big) \\
\frac{\eta^{\beta\gamma}_{3311}(r)}{k_{0\beta}re^{-r/a}} =& A_{rr}(k_{0\gamma}r)\big((\frac{1}{ra}+\frac{1}{a^2})\hbar^{2D}_{S2C2}(k_{0\beta}r) - \frac{1}{ra}\hbar^{2D}_{C2}(k_{0\beta}r)\big) \\
& - A_{\boldsymbol{I}}(k_{0\gamma}r)\big((\frac{1}{ra}+\frac{1}{a^2})\hbar^{2D}_{S2}(k_{0\beta}r) - \frac{1}{ra}\hbar^{2D}_{S0}(k_{0\beta}r)\big)
\end{aligned}
\tag{26}
$$

We remark that $\eta^{\beta\gamma}_{3131}(r) = \eta^{\beta\gamma}_{1331}(r) = \eta^{\beta\gamma}_{3113}(r) = \eta^{\beta\gamma}_{1313}(r)$. $\hbar^{2D}$ functions in (26)

are defined using Bessel functions of the first kind J_ν in the following way:

$$
\begin{aligned}
\hbar^{2D}_{S0}(y) &= \int_{\theta=0}^{2\pi} e^{iy\cos\theta}\,\mathrm{d}\theta = 2\pi J_0(y)\\
\hbar^{2D}_{C1}(y) &= \int_{\theta=0}^{2\pi} e^{iy\cos\theta}\cos\theta\,\mathrm{d}\theta = 2i\pi J_1(y)\\
\hbar^{2D}_{C2}(y) &= \int_{\theta=0}^{2\pi} e^{iy\cos\theta}\cos^2\theta\,\mathrm{d}\theta = 2\pi(y^{-1}J_1(y) - J_2(y))\\
\hbar^{2D}_{C3}(y) &= \int_{\theta=0}^{2\pi} e^{iy\cos\theta}\cos^3\theta\,\mathrm{d}\theta = 2i\pi(3y^{-1}J_2(y) - J_3(y))\\
\hbar^{2D}_{C4}(y) &= \int_{\theta=0}^{2\pi} e^{iy\cos\theta}\cos^4\theta\,\mathrm{d}\theta = 2\pi\big(-1+3y^{-2}\big)J_2(y)\\
\hbar^{2D}_{S2}(y) &= \int_{\theta=0}^{2\pi} e^{iy\cos\theta}\sin^2\theta\,\mathrm{d}\theta = 2\pi y^{-1}J_1(y)\\
\hbar^{2D}_{S4}(y) &= \int_{\theta=0}^{2\pi} e^{iy\cos\theta}\sin^4\theta\,\mathrm{d}\theta = 6\pi y^{-2}J_2(y)\\
\hbar^{2D}_{S2C1}(y) &= \int_{\theta=0}^{2\pi} e^{iy\cos\theta}\sin^2\theta\cos\theta\,\mathrm{d}\theta = 2i\pi y^{-1}J_2(y)\\
\hbar^{2D}_{S2C2}(y) &= \int_{\theta=0}^{2\pi} e^{iy\cos\theta}\sin^2\theta\cos^2\theta\,\mathrm{d}\theta = 2\pi(y^{-1}J_1(y) - 3y^{-2}J_2(y))
\end{aligned}
\tag{27}
$$

In the 3D case, after the analytical development of the integrals with respect to θ and φ, the fifteen integrands $\eta^{\beta\gamma}_{kmln}$ useful for the calculation of $\alpha^{\beta\gamma}_{klmn}$,

without the part $\frac{\langle \delta C_{j^\beta jkl} \delta C_{mnj^\beta j} \rangle}{2C^0_{j^\beta jj^\beta j}} \frac{(1-c(\gamma))}{4\pi\rho\omega^2}$, can be expressed as follows:

$$
\begin{aligned}
\frac{\eta^{\beta\gamma}_{3333}(r)}{k_{0\beta}r^2e^{-r/a}} =& 2\pi A_{rr}(k_{0\gamma}r)\big((\frac{1}{ra}+\frac{1}{a^2})\hbar^{3D}_{C4S1}(k_{0\beta}r) - \frac{2ik_{0\beta}}{a}\hbar^{3D}_{C3S1}(k_{0\beta}r) - (k^2_{0\beta}+\frac{1}{ra})\hbar^{3D}_{C2S1}(k_{0\beta}r)\big) \\
& -2\pi A_{\boldsymbol{I}}(k_{0\gamma}r)\big((\frac{1}{ra}+\frac{1}{a^2})\hbar^{3D}_{C2S1}(k_{0\beta}r) - \frac{2ik_{0\beta}}{a}\hbar^{3D}_{C1S1}(k_{0\beta}r) - (k^2_{0\beta}+\frac{1}{ra})\hbar^{3D}_{S1}(k_{0\beta}r)\big) \\
\frac{\eta^{\beta\gamma}_{1111}(r)}{k_{0\beta}r^2e^{-r/a}} =& A_{rr}(k_{0\gamma}r)\big(\frac{3\pi}{4}(\frac{1}{ra}+\frac{1}{a^2})\hbar^{3D}_{S5}(k_{0\beta}r) - \pi\frac{1}{ra}\hbar^{3D}_{S3}(k_{0\beta}r)\big) \\
& -A_{\boldsymbol{I}}(k_{0\gamma}r)\big(\pi(\frac{1}{ra}+\frac{1}{a^2})\hbar^{3D}_{S3}(k_{0\beta}r) - 2\pi\frac{1}{ra}\hbar^{3D}_{S1}(k_{0\beta}r)\big) \\
\frac{\eta^{\beta\gamma}_{1122}(r)}{k_{0\beta}r^2e^{-r/a}} =& A_{rr}(k_{0\gamma}r)\big(\frac{\pi}{4}(\frac{1}{ra}+\frac{1}{a^2})\hbar^{3D}_{S5}(k_{0\beta}r) - \pi\frac{1}{ra}\hbar^{3D}_{S3}(k_{0\beta}r)\big) \\
& -A_{\boldsymbol{I}}(k_{0\gamma}r)\big(\pi(\frac{1}{ra}+\frac{1}{a^2})\hbar^{3D}_{S3}(k_{0\beta}r) - 2\pi\frac{1}{ra}\hbar^{3D}_{S1}(k_{0\beta}r)\big) \\
\frac{\eta^{\beta\gamma}_{1212}(r)}{k_{0\beta}r^2e^{-r/a}} =& \frac{\pi}{4}A_{rr}(k_{0\gamma}r)(\frac{1}{ra}+\frac{1}{a^2})\hbar^{3D}_{S5}(k_{0\beta}r) \\
\frac{\eta^{\beta\gamma}_{1313}(r)}{k_{0\beta}r^2e^{-r/a}} =& \pi A_{rr}(k_{0\gamma}r)\big((\frac{1}{ra}+\frac{1}{a^2})\hbar^{3D}_{S3C2}(k_{0\beta}r) - \frac{ik_{0\beta}}{a}\hbar^{3D}_{S3C1}(k_{0\beta}r)\big) \\
\frac{\eta^{\beta\gamma}_{1133}(r)}{k_{0\beta}r^2e^{-r/a}} =& \pi A_{rr}(k_{0\gamma}r)\big((\frac{1}{ra}+\frac{1}{a^2})\hbar^{3D}_{S3C2}(k_{0\beta}r) - \frac{2ik_{0\beta}}{a}\hbar^{3D}_{S3C1}(k_{0\beta}r) - (k^2_{0\beta}+\frac{1}{ra})\hbar^{3D}_{S3}(k_{0\beta}r)\big) \\
& -2\pi A_{\boldsymbol{I}}(k_{0\gamma}r)\big((\frac{1}{ra}+\frac{1}{a^2})\hbar^{3D}_{S1C2}(k_{0\beta}r) - \frac{2ik_{0\beta}}{a}\hbar^{3D}_{S1C1}(k_{0\beta}r) - (k^2_{0\beta}+\frac{1}{ra})\hbar^{3D}_{S1}(k_{0\beta}r)\big) \\
\frac{\eta^{\beta\gamma}_{3311}(r)}{k_{0\beta}re^{-r/a}} =& A_{rr}(k_{0\gamma}r)\big(\pi(\frac{1}{ra}+\frac{1}{a^2})\hbar^{3D}_{S3C2}(k_{0\beta}r) - 2\pi\frac{1}{ra}\hbar^{3D}_{S1C2}(k_{0\beta}r)\big) \\
& -A_{\boldsymbol{I}}(k_{0\gamma}r)\big(\pi(\frac{1}{ra}+\frac{1}{a^2})\hbar^{3D}_{S3}(k_{0\beta}r) - 2\pi\frac{1}{ra}\hbar^{3D}_{S1}(k_{0\beta}r)\big)
\end{aligned}
\tag{28}
$$

We remark that $\eta^{\beta\gamma}_{2222}(r) = \eta^{\beta\gamma}_{1111}(r)$, $\eta^{\beta\gamma}_{2211}(r) = \eta^{\beta\gamma}_{1122}(r)$, $\eta^{\beta\gamma}_{1221}(r) = \eta^{\beta\gamma}_{2112}(r) = \eta^{\beta\gamma}_{2121}(r) = \eta^{\beta\gamma}_{1212}(r)$, and $\eta^{\beta\gamma}_{3n3n}(r) = \eta^{\beta\gamma}_{n33n}(r) = \eta^{\beta\gamma}_{3nn3}(r) = \eta^{\beta\gamma}_{n3n3}(r)$ for $n = 1, 2$, and $\eta^{\beta\gamma}_{3131}(r) = \eta^{\beta\gamma}_{3232}(r)$. $\hbar^{3D}$ functions in (28) are defined in the following way:

$$
\begin{aligned}
\hbar^{3D}_{S1}(y) &= \int_{\varphi=0}^{\pi} e^{iy\cos\varphi}\sin\varphi\,\mathrm{d}\varphi = 2y^{-1}\sin(y)\\
\hbar^{3D}_{S3}(y) &= \int_{\varphi=0}^{\pi} e^{iy\cos\varphi}\sin^3\varphi\,\mathrm{d}\varphi = 4(-y^{-2}\cos(y)+y^{-3}\sin(y))\\
\hbar^{3D}_{S5}(y) &= \int_{\varphi=0}^{\pi} e^{iy\cos\varphi}\sin^5\varphi\,\mathrm{d}\varphi = -16(3y^{-4}\cos(y)+(-3+y^2)y^{-5}\sin(y))\\
\hbar^{3D}_{C1S1}(y) &= \int_{\varphi=0}^{\pi} e^{iy\cos\varphi}\cos\varphi\sin\varphi\,\mathrm{d}\varphi = 2i(-y^{-1}\cos(y)+y^{-2}\sin(y))\\
\hbar^{3D}_{C2S1}(y) &= \int_{\varphi=0}^{\pi} e^{iy\cos\varphi}\cos^2\varphi\sin\varphi\,\mathrm{d}\varphi = 2(2y^{-2}\cos(y)+(-2+y^2)y^{-3}\sin(y))\\
\hbar^{3D}_{C3S1}(y) &= \int_{\varphi=0}^{\pi} e^{iy\cos\varphi}\cos^{\underline{2}3}\varphi\sin\varphi\,\mathrm{d}\varphi = 2i((6-y^2)y^{-3}\cos(y)+3(-2+y^2)y^{-4}\sin(y))\\
\hbar^{3D}_{C4S1}(y) &= \int_{\varphi=0}^{\pi} e^{iy\cos\varphi}\cos^{\underline{2}4}\varphi\sin\varphi\,\mathrm{d}\varphi = 2(4(-6+y^2)y^{-4}\cos(y)+(24-12y^2+y^4)y^{-5}\sin(y))\\
\hbar^{3D}_{S3C1}(y) &= \int_{\varphi=0}^{\pi} e^{iy\cos\varphi}\sin^{\underline{2}3}\varphi\cos\varphi\,\mathrm{d}\varphi = -4i(3y^{-3}\cos(y)+(-3+y^2)y^{-4}\sin(y))\\
\hbar^{3D}_{S4C1}(y) &= \int_{\varphi=0}^{\pi} e^{iy\cos\varphi}\sin^{\underline{2}4}\varphi\cos\varphi\,\mathrm{d}\varphi = -4((-12+y^2)y^{-4}\cos(y)-(-12+5y^2)y^{-5}\sin(y))
\end{aligned}
\tag{29}
$$

Figure 12 presents, for both 2D and 3D cases, the integrands $f^{L}_{klmn}(r) = f^{LL}_{klmn}(r)+f^{LT}_{klmn}(r)$, defined in (25) and after analytical integration with respect to θ in 2D and to (θ,φ) in 3D, plotted at three different frequencies, in order to illustrate how they evolve with respect to r.

For both 2D and 3D cases, the two developed integration methods give almost the same results. For example, the relative difference between them in 2D is less than 0.0006% for both longitudinal and transverse waves. As expected, the second method is shown to be much more stable and rapid than the first one, especially in the 3D case. Specifically, it takes about 30 minutes for 2D analysis and a few hours for 3D analysis by using the first method, while both 2D and 3D numerical analysis can be finished within one minute by using the

second method.

Appendix A2. Effects of anisotropy and inhomogeneity degrees of a polycrystalline material on the attenuation level

In order to have a preliminary understanding on the effects of anisotropy and inhomogeneity degrees of a polycrystalline material on the attenuation level, we compare here the attenuation coefficient of the following three materials with cubic-symmetry: the β-titanium considered in the present work, an Inconel 600 studied in [25], and a fictitious material defined in [33]. The characteristics of these materials are presented in Table III.

In our work we use ϵ_β ($\beta = L, T$) to define the inhomogeneity degrees of respectively the longitudinal and the transverse wave propagation constants in a polycrystalline material. They come from the work by Stanke and Kino [4] and are defined as follows:

$$\begin{aligned} \epsilon_L &= \sqrt{\frac{4}{525}}\frac{C_{11}-C_{12}-2C_{44}}{C_{11}^0} = \sqrt{\frac{4}{525}}(1-A)\frac{C_{11}-C_{12}}{C_{11}^0} \\ \epsilon_T &= \sqrt{\frac{3}{700}}\frac{C_{11}-C_{12}-2C_{44}}{C_{44}^0} = \sqrt{\frac{3}{700}}(1-A)\frac{C_{11}-C_{12}}{C_{44}^0} \end{aligned} \tag{30}$$

In (30), A denotes a degree of elastic anisotropy for crystals of cubic symmetry defined by Zener [40, 41] as:

$$A = \frac{C_{44}}{C_{11}-C_{12}} \tag{31}$$

A comparison between the longitudinal wave attenuation coefficients is presented in Figure 13 for the three materials, calculated both in 2D and in 3D. Firstly, the overall evolution of these curves are very similar for both 2D and 3D cases, which validate our discussion for the only titanium. To go in more detail, in the Rayleigh region, both anisotropy and inhomogeneity degrees A and ϵ_L have an insignificant effect on the attenuation coefficient. Maybe a higher anisotropy degree A leads to a slightly higher attenuation of the longitudinal wave. This is consistent with our conclusion that the Rayleigh scattering depends on the grain volume, involving all space directions, so the anisotropy degree of crystallite is the pertinent parameter to consider. On another hand, in the stochastic region, the higher the inhomogeneity degree ϵ_L, the higher the longitudinal attenuation level. This was expected taking into account dependency of the stochastic scattering for the longitudinal waves on the average

grain length along the propagation direction. So the inhomogeneity degree of the propagation constant significantly influences the attenuation level.

Materials	C_{11} (GPa)	C_{12} (GPa)	C_{44} (GPa)	A	$\epsilon_L(\%)$	$\epsilon_T(\%)$	ρ (kg/m^3)
β-titanium: Single crystallite in cubic axes	134.0	110.0	36.0	3.00	2.74	8.73	4428
β-titanium: Voigt-averaged homogeneous medium	150.0	100.0	26.5	0	0	0	4428
Inconel600 [25]: Single crystallite in cubic axes	234.6	145.4	126.2	2.83	4.8	15.23	8260
Inconel600 [25]: Voigt-averaged homogeneous medium	300.0	112.8	93.6	0	0	0	8260
Fictitious material [33]: Single crystallite in cubic axes	237.1	149.0	107.8	2.40	3.87	10.15	8000
Fictitious material [33]: Voigt-averaged homogeneous medium	288.1	123.5	82.3	0	0	0	8000

Table III: Elastic properties for three different polycrystalline materials with cubic symmetry.

References

[1] T. Garcin, J. H. Schmitt, M. Militzer, In-situ laser ultrasonic grain size measurement in superalloy INCONEL 718, Journal of Alloys and Compounds 670 (2016) 329–336.

[2] M. Keyvani, T. Garcin, D. Fabrègue, M. Militzer, K. Yamanaka, A. Chiba, Continuous measurements of recrystallization and grain growth in cobalt super alloys, Metallurgical and Materials Transactions A 48 (5) (2017) 2363–2374.

[3] F. Dong, X. Wang, Q. Yang, A. Yin, X. Xu, Directional dependence of aluminum grain size measurement by laser-ultrasonic technique, Materials Characterization 129 (2017) 114–120.

[4] F. E. Stanke, G. S. Kino, A unified theory for elastic wave-propagation in polycrystalline materials, J. Acoust. Soc. Amer. 75(3) (1984) 665–681.

[5] L. Botvina, L. J. Fradkin, B. Bridge, A new method for assessing the mean grain size of polycrystalline materials using ultrasonic nde, Journal of materials science 35 (18) (2000) 4673–4683.

[6] A. B. Bhatia, Scattering of high-frequency sound waves in polycrystalline materials, J. Acoust. Soc. Amer. 31 (1959) 16–23.

[7] A. Bhatia, R. Moore, Scattering of high-frequency sound waves in polycrystalline materials ii, J. Acoust. Soc. Amer. 31 (1959) 1140–1141.

[8] S. Hirsekorn, The scattering of ultrasonic-waves by polycrystals, J. Acoust. Soc. Amer. 72 (1982) 1021–1031.

[9] F. C. Karal, J. B. Keller, Elastic, Electromagnetic, and Other Waves in Random Medium, Journal of Mathematical Physics 5 (1964) 537–547.

[10] R. L. Weaver, Diffusivity of ultrasound in polycrystals, Journal of the Mechanics and Physics of Solids 38 (1990) 55–86.

[11] C. M. Kube, Iterative solution to bulk wave propagation in polycrystalline materials., Journal of the Acoustical Society of America 141 (3) (2017) 1804–1811.

[12] J. A. Turner, Elastic wave propagation and scattering in heterogeneous, anisotropic media: Textured polycrystalline materials, Journal of the Acoustical Society of America 106 (2) (1999) 541–552.

[13] L. Yang, O. I. Lobkis, S. I. Rokhlin, Shape effect of elongated grains on ultrasonic attenuation in polycrystalline materials, Ultrasonics 51 (2011) 697–708.

[14] A. P. Arguelles, J. A. Turner, Ultrasonic attenuation of polycrystalline materials with a distribution of grain sizes, The Journal of the Acoustical Society of America 141 (6) (2017) 4347–4353.

[15] A. Van Pamel, C. R. Brett, P. Huthwaite, M. J. S. Lowe, Finite element modelling of elastic wave scattering within a polycrystalline material in two and three dimensions, J. Acoust. Soc. Amer. 138 (2015) 2326–2336.

[16] A. Van Pamel, P. Nagy, M. J. S. Lowe, On the dimensionality of elastic wave scattering within heterogeneous media, J. Acoust. Soc. Amer. 140 (2016) 4360–4366.

[17] B. Tie, D. Solas, J. Thébault, C. Rey, T. Baudin, A. Mouronval, Modélisation numérique de la propagation des ultrasons dans des milieux polycristallins, in: 10th French Congress of Acoustics (CFA2010), https://hal.archives-ouvertes.fr/hal-00550917 (in French), Lyon, France, Avril 2010, p. 6 pages.

[18] S. Shahjahan, F. Rupin, A. Aubry, B. Chassignole, T. Fouquet, A. Derode, Comparison between experimental and 2-d numerical studies of multiple scattering in inconel600®; by means of array probes, Ultrasonics 54 (1) (2014) 358–367.

[19] B. Chassignole, V. Duwig, M. A. Ploix, P. Guy, G. R. El, Modelling the attenuation in the athena finite elements code for the ultrasonic testing of austenitic stainless steel welds., Ultrasonics 49 (8) (2009) 653–658.

[20] X. Bai, B. Tie, J.-H. Schmitt, D. Aubry, Finite element modeling of grain size effects on the ultrasonic microstructural noise backscattering in polycrystalline materials, Ultrasonics 87 (2018) 182–202.

[21] J. H. Rose, Ultrasonic backscatter from microstructure, in: Review of Progress in Quantitative Nondestructive Evaluation. Vol. 11B, Vol. 11, 1992, pp. 1677–1684.

[22] A. C. Eringen, E. S. Suhubi, Elastodynamics. 2, Linear theory, Academic Press, New York, 1975.

[23] J. E. Gubernatis, E. Domany, J. A. Krumhansl, Formal aspects of theory of scattering of ultrasound by flaws in elastic-materials, Journal of Applied Physics 48 (1977) 2804–2811.

[24] C. M. Kube, J. A. Turner, Acoustic attenuation coefficients for polycrystalline materials containing crystallites of any symmetry class, J. Acoust. Soc. Amer. 137 (6) (2015) EL476–EL482.

[25] M. Ryzy, T. Grabec, P. Sedlák, I. A. Veres, Influence of grain morphology on ultrasonic wave attenuation in polycrystalline media with statistically equiaxed grains, Journal of the Acoustical Society of America 143 (1) (2018) 219.

[26] F. J. Margetan, L. X. Yu, R. B. Thompson, Computation of grain-noise scattering coefficients for ultrasonic pitch/catch inspections of metals, in: D. Thompson, D. Clementi (Eds.), Review of Progress in Quantitative Nondestructive Evaluation, Vol. 24, American Institute of Physics, 2005, pp. 1300–1307.

[27] F. E. Stanke, Spatial autocorrelation functions for calculations of effective propagation constants in polycrystalline materials, Journal of the Acoustical Society of America 80 (5) (1986) 1479–1485.

[28] W. Petry, A. Heiming, J. Trampenau, M. Alba, C. Herzig, H. R. Schober, G. Vogl, Phonon dispersion of the bcc phase of group-iv metals. i. bcc titanium., Phys Rev B Condens Matter 43 (13) (1991) 10933–10947.

[29] B. Tie, D. Aubry, Adaptive time discontinuous galerkin method for numerical modelling of wave propagation in shell and 3D structures, European Journal of Computational Mechanics 15 (6) (2006) 729–757.

[30] T. J. Hughes, G. M. Hulbert, Space-time finite element methods for elastodynamics: Formulations and error estimates, Computer Methods in Applied Mechanics and Engineering 66 (3) (1988) 339 – 363.

[31] X. D. Li, N. E. Wiberg, Implementation adaptivity of a space-time finite element method for structural dynamics, Computer Methods in Applied Mechanics and Engineering 156 (1) (1998) 211–229.

[32] A. Van Pamel, G. Sha, S. I. Rokhlin, M. J. S. Lowe, Finite-element modelling of elastic wave propagation and scattering within heterogeneous media, Proceedings of the Royal Society of London A: Mathematical, Physical and Engineering Sciences 473 (2197).

[33] A. V. Pamel, G. Sha, M. J. S. Lowe, S. I. Rokhlin, Numerical and analytic modelling of elastodynamic scattering within polycrystalline materials, Journal of the Acoustical Society of America 143 (4) (2018) 2394–2408.

[34] A. V. Pamel, P. Huthwaite, C. R. Brett, M. J. S. Lowe, Numerical simulations of ultrasonic array imaging of highly scattering materials, Ndt&E International 81 (2016) 9–19.

[35] J. A. Turner, G. Ghoshal, Simulations of elastic wave propagation through voronoi polycrystals, Journal of the Acoustical Society of America 112 (5) (2002) 2439–2439.

[36] G. Ghoshal, J. A. Turner, Numerical model of longitudinal wave scattering in polycrystals, IEEE Transactions on Ultrasonics Ferroelectrics and Frequency Control 56 (7) (2009) 1419–1428.

[37] S. Ghosh, Z. Nowak, K. Lee, Tessellation-based computational methods for the characterization and analysis of heterogeneous microstructures, Composites Science and Technology 57 (9-10) (1997) 1187–1210.

[38] S. Kumar, S. K. Kurtz, J. R. Banavar, M. G. Sharma, Properties of a three-dimensional poisson-voronoi tesselation: A monte carlo study, Materials Characterization 71 (1-2) (1993) 349–349.

[39] X. Bai, Finite element modeling of ultrasonic wave propagation in polycrystalline materials, Ph.D. thesis, CentraleSupélec, Université Paris-Saclay, codirection avec Denis Aubry (MSSMat) et Jean-Hubert Schmitt (MSSMat) (2017).

[40] C. Zener, Elasticity and Anelasticity of Metals, University of Chicago, Chicago, 1948.

[41] C. M. Kube, Elastic anisotropy of crystals, AIP Advances 6 (2016) 095209.

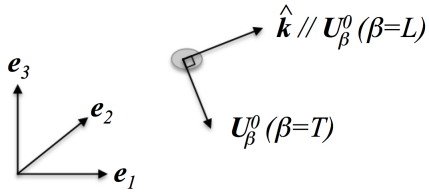

Figure 1: Sketch showing in the 3D case the unit vector of propagation direction $\hat{\boldsymbol{k}}$ and the polarization vectors $\boldsymbol{U}_\beta^0$ within the orthonormal basis $\{\boldsymbol{e}_m\}_{m=1,\cdots,3}$.

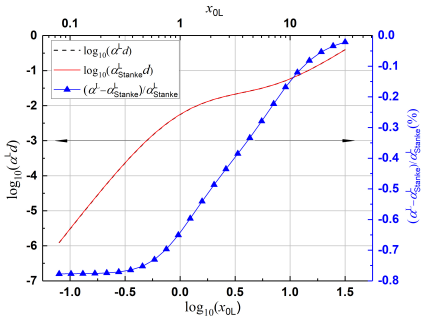

Figure 2: Comparison in 3D between the longitudinal wave attenuation coefficient α^L_{Stanke} by Stanke and Kino [4] and α^L calculated with the explicite formula (15).

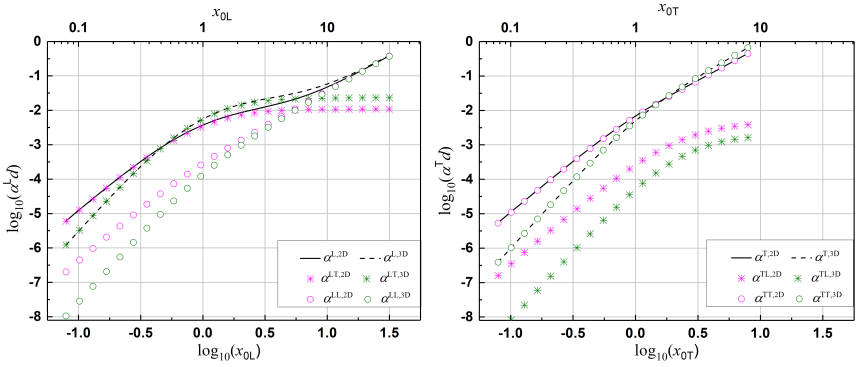

(a) (b)

Figure 3: Evolution of αd the attenuation per crystallite with respect to x_0 the normalized frequency for (a) longitudinal waves and (b) traverse waves, respectively, in a $\beta-$titanium polycrystal: comparison between 2D and 3D calculations, and contribution of the scattering modes to the attenuation.

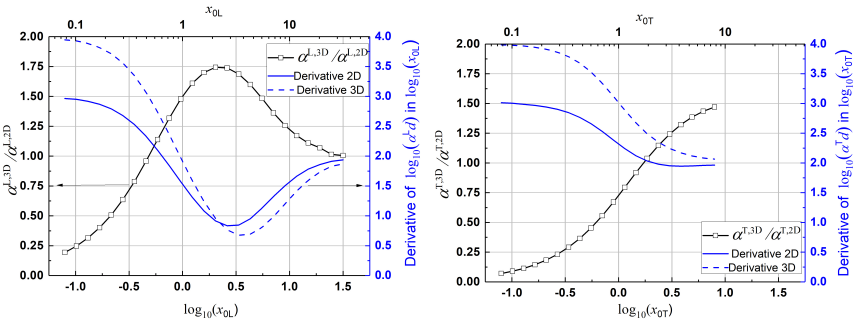

(a) (b)

Figure 4: Evolution of the ratio of attenuation coefficients calculated in 3D and 2D (left axis in black) and the derivative of $log_{10}(\alpha d)$ w.r.t. $log_{10}(x_0)$, *i.e.* the exponent n value (right axis in blue), for (a) longitudinal waves and (b) transverse waves, respectively, in a $\beta-$titanium polycrystal.

831

832

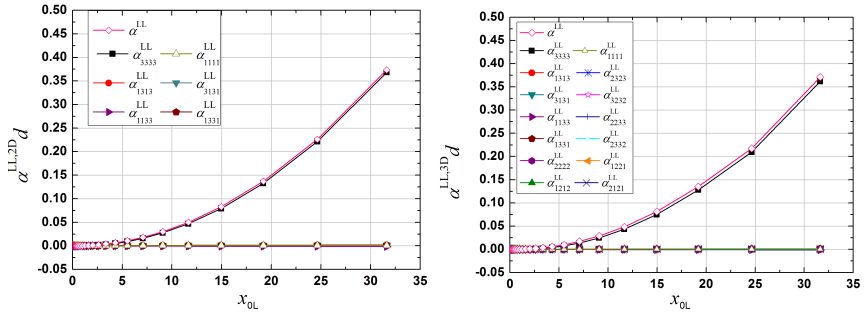

(a) (b)

Figure 5: Evolution of the longitudinal-to-longitudinal wave scattering-induced attenuation, α^{LL}_{klmn}, w.r.t. the normalized frequency in (a) 2D and (b) 3D case.

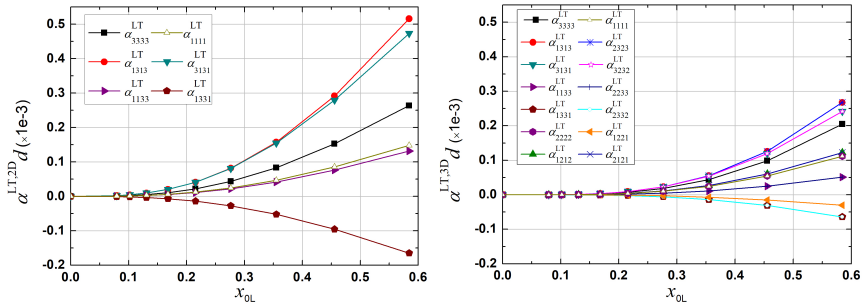

(a) (b)

Figure 6: Evolution of the longitudinal-to-transverse wave scattering-induced attenuation, α^{LT}_{klmn}, w.r.t. the normalized frequency in (a) 2D and (b) 3D case.

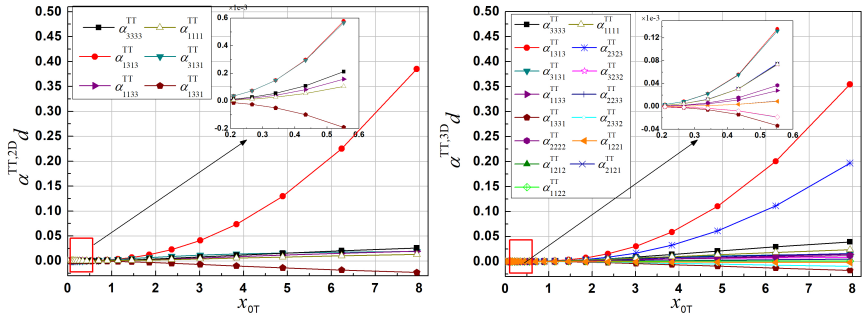

(a) (b)

Figure 7: Evolution of the transverse-to-transverse wave scattering-induced attenuation, α^{TT}_{klmn}, w.r.t. the normalized frequency in (a) 2D and (b) 3D case, with furthermore an enlarged view at low frequencies in the Rayleigh region $x_{0T} \in]0.2, 0.6[$.

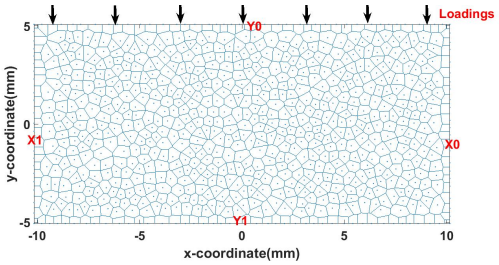

Figure 8: Illustration of the 2D FE model with a Voronoï-type polycrystalline microstructure.

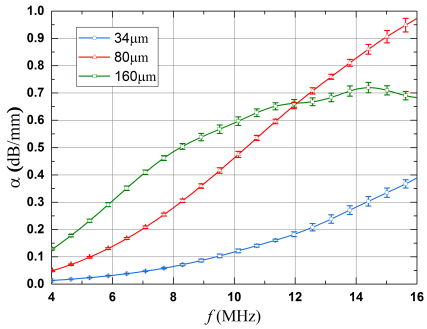

Figure 9: Standard deviation (bars) and mean (solid circles) estimations of the attenuation coefficient versus frequency for a longitudinal wave in a β-titanium polycrystal with three different grain sizes.

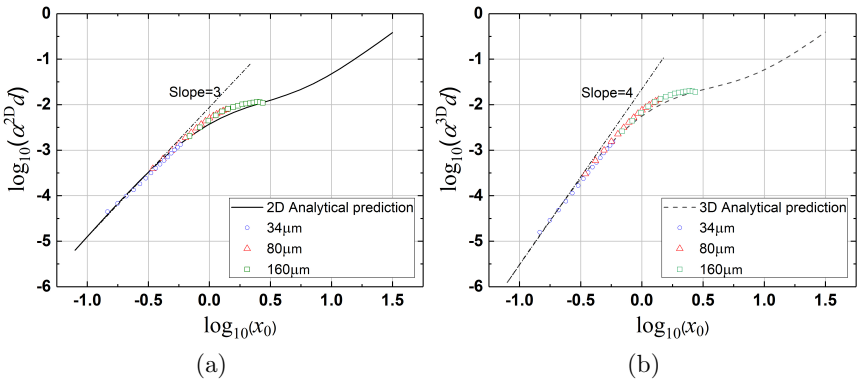

Figure 10: Numerical estimations for normalized attenuation coefficient versus normalized frequency using logarithmic scales, $log_{10}(\alpha d)$ vs. $log_{10}(x_0)$, for a longitudinal wave in a β-titanium polycrystal with three different grain sizes: (a) the 2D results and (b) the deduced 3D results based on the ratio of analytical attenuation between 2D and 3D models α^{3D}/α^{2D}, compared to the analytical predictions.

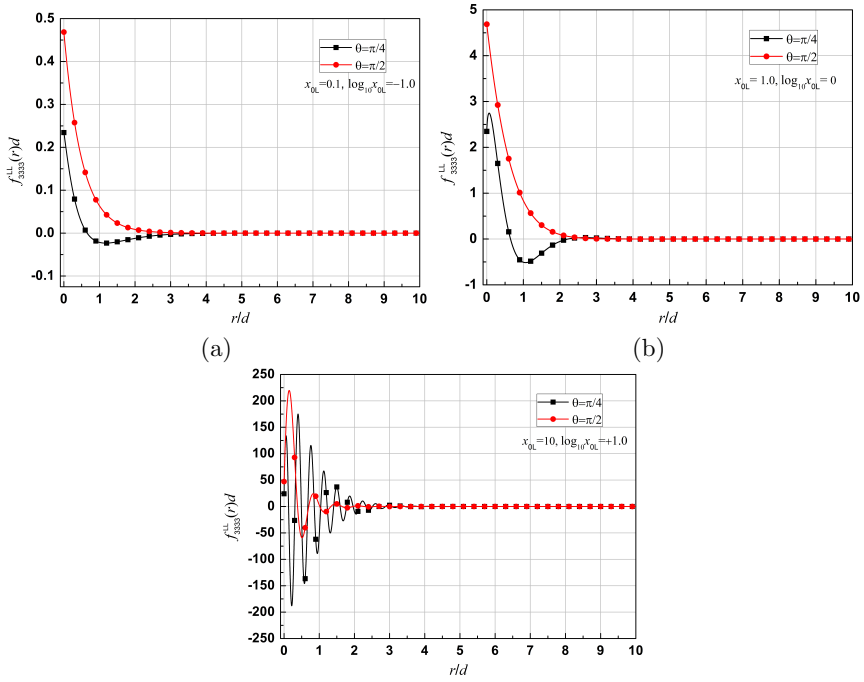

Figure 11: In the 2D case, normalized integrand function $f^{LL}_{3333}d$ as a function of the normalized integrand variable r/d in Eq.(25) at three different normalized frequencies (a) $x_{0L} = 0.1$, (b) $x_{0L} = 1.0$, and (c) $x_{0L} = 10$ for the grain size of $d = 80\mu$m, with $f^{LL}_{3333} \equiv \mathrm{Im}\left(\frac{k_{0\beta}\langle\delta C_{3333}\delta C_{3333}\rangle}{2C^0_{3333}} r G^L_{33}(r,\theta) D^L_{33}(r,\theta)\right)$ and for $\theta = \pi/4, \pi/2$.

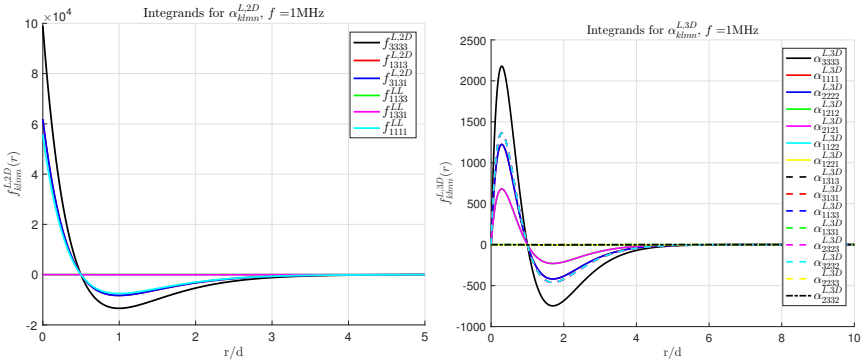

(a)

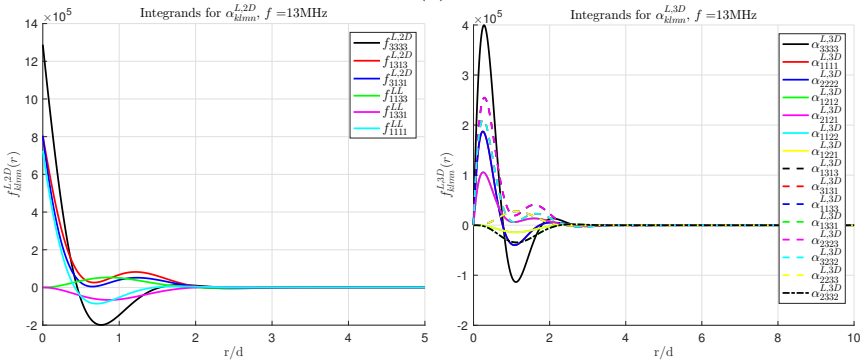

(b)

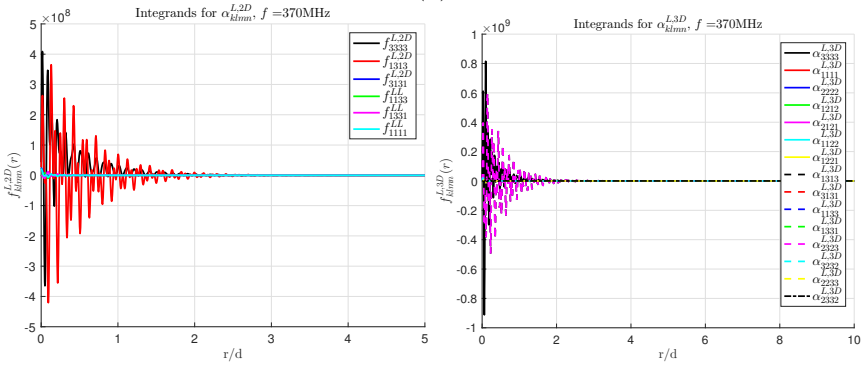

(c)

Figure 12: Integrands $f^{L}_{klmn}(r) = f^{LL}_{klmn}(r) + f^{LT}_{klmn}(r)$, defined in (25) and after analytical integration with respect to θ in 2D and to (θ, φ) in 3D, plotted at three different frequencies f = (a) 1MHz ($x_0 = 0.08$), (b) 13MHz ($x_0 = 1.0$), and (c) 370MHz ($x_0 = 32.2$) for the grain size of $d = 80\mu$m, with $f^{L}_{klmn} \equiv \mathrm{Im}\left(\frac{k_{0\beta}\langle \delta C_{33kl}\delta C_{mn33}\rangle}{2C^{0}_{3333}}\frac{1}{4\pi\rho\omega^2}(\eta^{LL}_{kmln} + \eta^{LT}_{kmln})\right)$

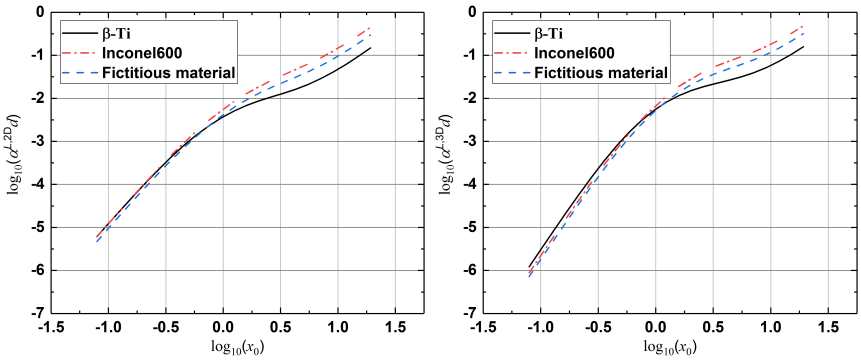

(a) (b)

Figure 13: Comparison of the longitudinal wave attenuation coefficient between three materials for both (a) 2D and (b) 3D cases